

University of Nevada, Reno

**Heat Transfer and Fan Power Performance of a Developing
Grooved Passage Flow Including Inlet and Exit Effects**

A thesis submitted in partial fulfillment of the
requirements for the degree of Master of Science in
Mechanical Engineering

by

John H. Akerley

Dr. Miles Greiner/Thesis Advisor

August 2012

Copyright by John H. Akerley 2012

All Rights Reserved



University of Nevada, Reno
Statewide • Worldwide

THE GRADUATE SCHOOL

We recommend that the thesis
prepared under our supervision by

JOHN H. AKERLEY

entitled

**Heat Transfer And Fan Power Performance Of A Developing Grooved Passage
Flow Including Inlet And Exit Effects**

be accepted in partial fulfillment of the
requirements for the degree of

MASTER OF SCIENCE

Miles Greiner, Ph. D., Advisor

Chanwoo Park, Ph. D., Committee Member

Dev Chidambaram, Ph. D., Graduate School Representative

Marsha H. Read, Ph. D., Dean, Graduate School

August, 2012

Abstract

Enhanced heat transfer surfaces are used frequently in a variety of practical devices. In the past, transverse surface grooves have shown promise in heat transfer augmentation. These lead to the formation of free shear layers and traveling waves, which augment convective transport normal to the passage walls. In the current work, two-dimensional Navier-Stokes simulations of heat and momentum transport using the spectral element technique are used to investigate the heat transfer and fan power performance of the developing regions of finite-length, grooved channel passage arrays. This study also considers the accelerating and decelerating flows entering and exiting the arrays. The computational domain has an inlet region followed by two passages stacked one above the other with thirty contiguous transverse grooves cut symmetrically into opposite walls and then a sufficiently long exit region that allows pressure recovery to take place. The performance metrics defined in the work include the average array Nusselt number and the total required fan power. The performance of the grooved channel arrays is compared with that of flat passage arrays with the same average wall center-to-center spacing (equal flow volume) for the Reynolds number range $1000 \leq Re \leq 3000$. The addition of grooves improves the overall heat transfer by a factor of 1.46 at $Re = 1000$ and by a factor of 2.75 at $Re = 3000$. The current calculations will provide guidance for future three-dimensional calculations of heat transfer versus fan power performance of developing flow within grooved passage arrays. Earlier studies show that three-dimensional results more accurately reproduce experimental results for Reynolds numbers greater than roughly 600.

Acknowledgements

I would first like to thank my advisor Professor Miles Greiner, Ph.D. for the opportunity to learn and grow as an engineer under his guidance.

I also would like to thank Dr. Paul Fischer and Dr. Aleksandr Obabko at Argonne National Laboratory for their guidance, and patience, while I delved into the world of computational fluid dynamics.

I would also like to thank my committee members, Dr. Chanwoo Park and Dr. Dev Chidambaram for their time being a part of my committee.

I would like to thank my family and friends. To my wife Kaite, your unwavering support has helped me accomplish my goals. To my parents, Tina and Holland, your guidance and support throughout my entire life have shaped the person I am today. I could not have succeeded without your constant love and encouragement.

Finally, I would like to acknowledge my funding under the University of Nevada, Reno Fellowship in Material and Thermal Sciences for Nuclear Power, contract NRC-38-10-949. Work on this project was additionally funded under U.S. Department of Energy contract DE-EE0003231.

Table of Contents

Abstract	i
Acknowledgements	ii
Table of Contents	iii
List of Tables	v
List of Figures	vi
Nomenclature	viii
1. Introduction	1
1.1 Background	1
1.2 Scope of Research	5
2. Two-Dimensional Array Model	7
2.1 Computational Domain	7
2.2 Spectral Element Method	11
2.3 Numerical Investigation	12
2.4 Onset of Oscillatory Flow	13
2.5 Heat Transfer Performance	16
2.6 Pressure Drop Analysis	23
2.7 Fan Power Performance	27
2.8 Summary	34

3. Two-Dimensional Single Channel	37
3.1 Domain Design.....	37
3.2 Heat Transfer Comparison	40
3.3 Fan Power Comparison	45
4. Conclusions and Recommendations.....	50
4.1 Conclusions	50
4.2 Recommendations	51
4.3 Recommended Three-Dimensional Model	52
References	54

List of Tables

Table 3-1.	Single channel and channel array average Nusselt number percent difference	43
Table 3-2.	Single channel and channel array non-dimensional fan power percent difference	48

List of Figures

Figure 1-1.	Industrial heat transfer equipment	4
Figure 1-2.	Comparing flat with grooved passage arrays	5
Figure 2-1.	Computational domain and spectral element mesh	8
Figure 2-2.	Spectral element mesh of inlet region and channel entrance for flat passage array	10
Figure 2-3.	Fluid vorticity contour plots	13
Figure 2-4.	Observed onset location of oscillatory flow	15
Figure 2-5.	Average Nusselt number versus groove coordinate	18
Figure 2-6.	Average Nusselt number resolution test	21
Figure 2-7.	Average full channel Nusselt number versus Reynolds number	23
Figure 2-8.	Heat exchanger core model for pressure-drop analysis from Kays and London [34]	25
Figure 2-9.	Non-dimensional pressure drop for $Re = 1000$	26
Figure 2-10.	Open thermodynamic system	27
Figure 2-11.	Non-dimensional fan power versus groove coordinate	30
Figure 2-12.	Fan power contributions versus Reynolds number	31
Figure 2-13.	Fan power contribution ratio versus Reynolds number	32

Figure 2-14.	Full channel non-dimensional fan power versus Reynolds number	33
Figure 2-15.	Full channel average Nusselt number versus full channel non-dimensional fan power	34
Figure 2-16.	Heat transfer enhancement ratio versus Reynolds number	35
Figure 2-17.	Fan power requirement ratio versus Reynolds number	36
Figure 3-1.	Two-dimensional, single channel mesh	38
Figure 3-2.	Total average Nusselt number versus dimensionless time	39
Figure 3-3.	Average Nusselt number array and single channel comparison	40
Figure 3-4.	Total average Nusselt number array and single channel comparison	44
Figure 3-5.	Non-dimensional fan power array and single channel comparison	45
Figure 3-6.	Total fan power array and single channel comparison	49
Figure 4-1.	Isometric view of three-dimensional, single channel mesh boundary	52

Nomenclature

A	Exchanger total heat transfer area on one side
A_c	Exchanger minimum free-flow area
A_{px}	Total projected surface area
a	Groove length
b	Groove depth
c_p	Fluid specific heat
C_{fP}	Poiseuille friction factor
$C_{f,app}$	Overall friction factor
D_H	Hydraulic diameter, $2H_A$
f	Mean friction factor
G	Exchanger flow-stream mass velocity
H_A	Average channel height
H_M	Minimum channel height
k	Fluid thermal conductivity
K_C	Contraction loss coefficient for flow at heat exchanger entrance

K_e	Expansion loss coefficient for flow at heat exchanger exit
K_∞	Pressure drop parameter
L	Channel length
L_E	Exit region length
L_I	Inlet region length
\dot{m}	Mass flow rate
Nu_L	Average Nusselt number at $x_G = 30$
Nu_x	Average Nusselt number between inlet and location x
P	Pressure
Pr	Fluid molecular Prandtl number, 0.70
Re	Reynolds number, $u_0(2H_m)/\nu$
Re_c	Critical Reynolds number
T	Temperature
T_0	Inlet temperature
T_w	Wall temperature
u	Axial velocity
u_0	Inlet axial velocity

v Velocity

v_m Mean velocity

v Specific volume

V Volume

w Wall thickness

W Flow work

x_G Groove coordinate, x/a

Greek

α Thermal diffusivity

ρ Fluid density

ν Fluid kinematic viscosity

Φ Non-dimensional fan power

Φ_{chan} Fan power contribution from within the grooved passage arrays

Φ_{i-e} Fan power contribution from the grooved passage inlet and exit effects

Φ_L Non-dimensional fan power at $x_G = 50$

Φ_{ratio} Fan power contribution ratio, Φ_{chan}/Φ_{i-e}

Φ_x Non-dimensional fan power at location x

σ	Ratio of free-flow area to frontal area
ζ	Graetz-type variable
χ_{FP}	Fan power requirement ratio
χ_{Nu}	Heat transfer enhancement ratio

Chapter 1: Introduction

1.1 Background

The need to increase efficiency in a variety of practical exchange devices, such as compact heat exchangers, power plant condensers, and heating, ventilation and air conditioning devices, has driven research in enhanced heat transfer surfaces and core modifications [1]. Standard, parallel-wall ducts that use moderately low Reynolds numbers are limited by the absence of convective mixing. As a result, the heat transfer levels of the systems that employ these standard heat exchanger configurations can be limited. Some heat transfer enhancement configurations rely on surface extension (fins) to increase the heat transfer surface area to volume ratio. Other configurations rely on the high heat transfer coefficients associated with boundary layer interruption (louvers and offset strips). These modifications are not specifically intended to modify the flow field itself.

In the past, researchers have performed numerical and experimental studies considering passage configurations that enhance mixing and heat transfer by triggering flow instabilities due to flow field modification. Transversely grooved channels [2-5], passages with eddy promoters [6,7], and communicating channels [8] all contain features whose sizes are roughly half the channel wall-to-wall spacing. These features lead to the formation of free shear layers that contain inflections in the passage velocity profile and feed energy to the least stable hydrodynamic instability modes. Kelvin-Helmholtz instabilities of these inflected profiles project energy onto normally-damped Tollmien-

Schlichting waves resulting in two-dimensional traveling waves at moderately low Reynolds numbers.

Numerical and experimental resonant heat transfer enhancement studies sparked an interest in destabilized flows in transversely grooved channels [3,9-11]. These focused on fully developed flows at laminar and transitional Reynolds numbers in rectangular cross-section channels with square grooves cut transversely into the walls. The flow rate was actively modulated near the natural frequency of the least stable Tollmien-Schlichting modes. Instabilities were observed at moderately low Reynolds numbers that significantly enhanced mixing and heat transfer. These studies concluded that a properly tuned 20-percent flow rate modulation could enhance heat transfer by a factor of two and a half [3,9]. However, this augmentation requires active flow modification, which is innately less reliable than passive enhancement techniques.

As a result, a series of experimental and numerical studies performed by Greiner et al. considered passive shear destabilized transport enhancement using saw-tooth transverse surface grooves [4,12-19]. The primary mechanism for enhancement within these passages is the excitation of normally-damped Tollmien-Schlichting waves within the flow [14]. Analyses of hydrodynamic instabilities show that Tollmien-Schlichting waves will grow in flat passages above a critical Reynolds number, Re_c , of 15,400 [20]. However, most applications cannot utilize these waves since three-dimensional turbulence, which begins after a Reynolds number of 2800 in flat passages, masks them. Experiments have shown that the addition of transverse surface grooves whose length is compatible with the most slowly decaying Tollmien-Schlichting mode considerably

reduces the critical Reynolds number for the onset of waves [13]. Visualizations in a range of passage geometries with fully developed flow show that the critical Reynolds number where two-dimensional waves first appear decreases as the spacing between grooves decreases. For a sawtooth-shaped wall with no spacing between grooves, two-dimensional waves first appear at $Re_c = 350$, followed by a transition to three-dimensional mixing at Reynolds numbers greater than 500 [13].

Numerical and experimental investigations using air in a fully developed flow show that both the Nusselt number and friction factor are greater than the corresponding values for a flat channel with the same minimum wall-to-wall spacing [4,19]. Three-dimensional numerical simulations for $Re \leq 2000$ give results that are in good agreement with experimental measurements [15,16]. However, two-dimensional simulations were inadequate for capturing the transport processes in these configurations for Reynolds numbers greater than $Re = 570$ [15].

Air passage lengths in some practical heat transfer devices are less than fifty times the wall center-to-center spacing in order to take advantage of the high heat transfer coefficients associated with developing flow. When a uniform flow of constant temperature enters an elevated-temperature channel, the thermal boundary layer is small and grows further downstream. The small thermal boundary layer allows the fast moving, cool air to contact the heated walls. As the boundary layer grows, the heat transfer and shear stress decrease to a constant value and the flow becomes fully-developed. To reach a fully-developed flow at a Reynolds number of 1000, it takes roughly 60 hydraulic diameters [21]. Figure 1-1 shows one example of a heat exchanger

[22]. Blowers are used to force air through passages that are brazed to the outer surface of tubes carrying the working fluid that is being condensed. Furthermore, the low thermal conductivity, specific heat, and density of the air inhibit its ability to remove heat from the passage walls as compared to water, but water is not available in many locations for cooling. As a result, the air side of heat exchangers can limit the overall performance of the system.

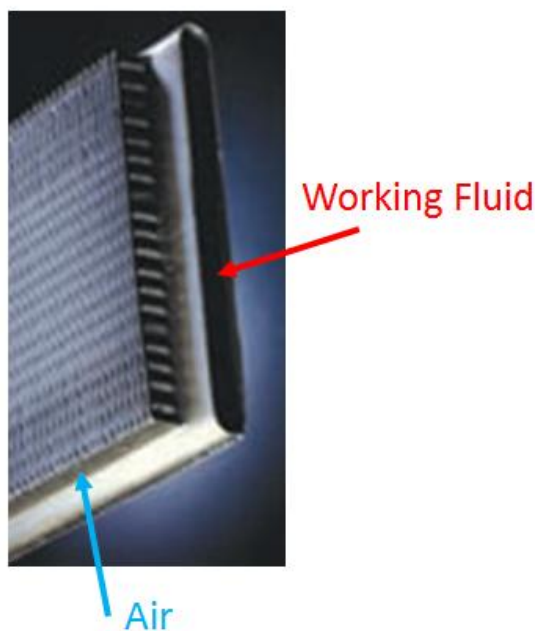


Figure 1-1. Industrial heat transfer equipment.

In recent years, researchers have given attention to other groove shapes or surface additions that limit the pressure drop within the air side channel. Studies have shown that semispherical dimples impressed on the surface of parallel-plate passages produced significant heat transfer augmentation with relatively small pressure drop [23,24]. The addition of curved vanes to grooved passages has also shown a reduction in pressure drop

for Reynolds numbers of less than 400 [25,26]. The current work, however, returns to the sawtooth-geometry intended to destabilize the slowest decaying Tollmien-Schlichting waves [13].

Previous analyses focused on heat transfer augmentation with fully developed flow. However, the configurations shown in Figure 1-1 indicate that developing flow is important in practical passages and that the flow experiences significant acceleration at the channel entrance (due to the wall thickness and shape) and deceleration at its exit. Furthermore, since these devices use arrays of parallel passages, the interaction of the entrance and exit regions of neighboring grooved passages must be examined, which to our knowledge has yet to be done.

1.2 Scope of Research

The current work is a numerical investigation of heat and momentum transport in finite-length continuously grooved passages with developing flow. Figure 1-2 shows a comparison of a flat passage array with a grooved passage array with the same average wall center-to-center spacing and flow volume.

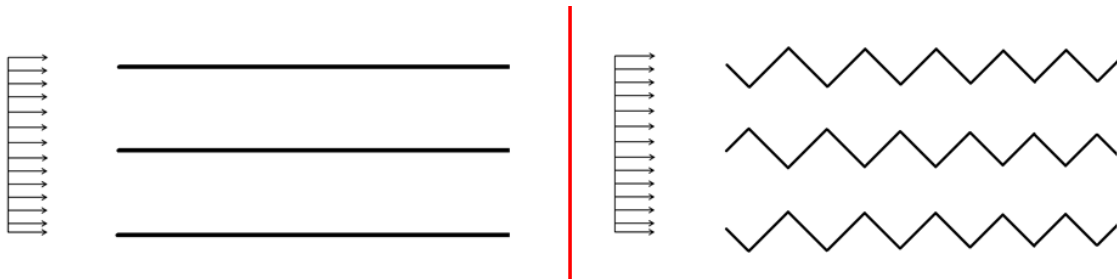


Figure 1-2. Comparing flat with grooved passage arrays.

Analyses will focus on arrays where flow accelerates into the passages, develops within the passages, and then diffuses outside of the passages. The performance of these passages is analyzed using the average Nusselt number and fan power required to move the air through the passages. These results are compared with arrays with flat passages of equal wall center-to-center spacing and equal wall mass per volume.

Chapter 2: Two-Dimensional Array Model

2.1 Computational Domain

Figure 2-1 shows the two-dimensional spectral element mesh used in the current work to study an array of grooved passages. A flow of air with Prandtl number 0.7 enters the left side of the entrance region (length of region is $L_I = 2.5 a$) with a uniform dimensionless axial speed of $u_0 = 1$ and dimensionless temperature of $T_0 = 0$. The flow then encounters a pair of grooved channels (one above the other) at location $x = 0$ with length $L = 30 a$. The passage walls are indicated on Figure 2-1 with bold black lines and are modeled using no-slip velocity conditions and a uniform dimensionless temperature of $T_w = 1$. The flow exits the channel array into an exit region of length $L_E = 25 a$. Due to the large domain size, Figure 2-1 shows a break in the channel array and in the exit region. Periodic boundary conditions are applied to the upper and lower edges of the inlet and exit regions to model an infinite number of channels stacked above and below the computational domain (the zigzag shape of the region boundaries are used for convenience, but flat boundaries would be equivalent).

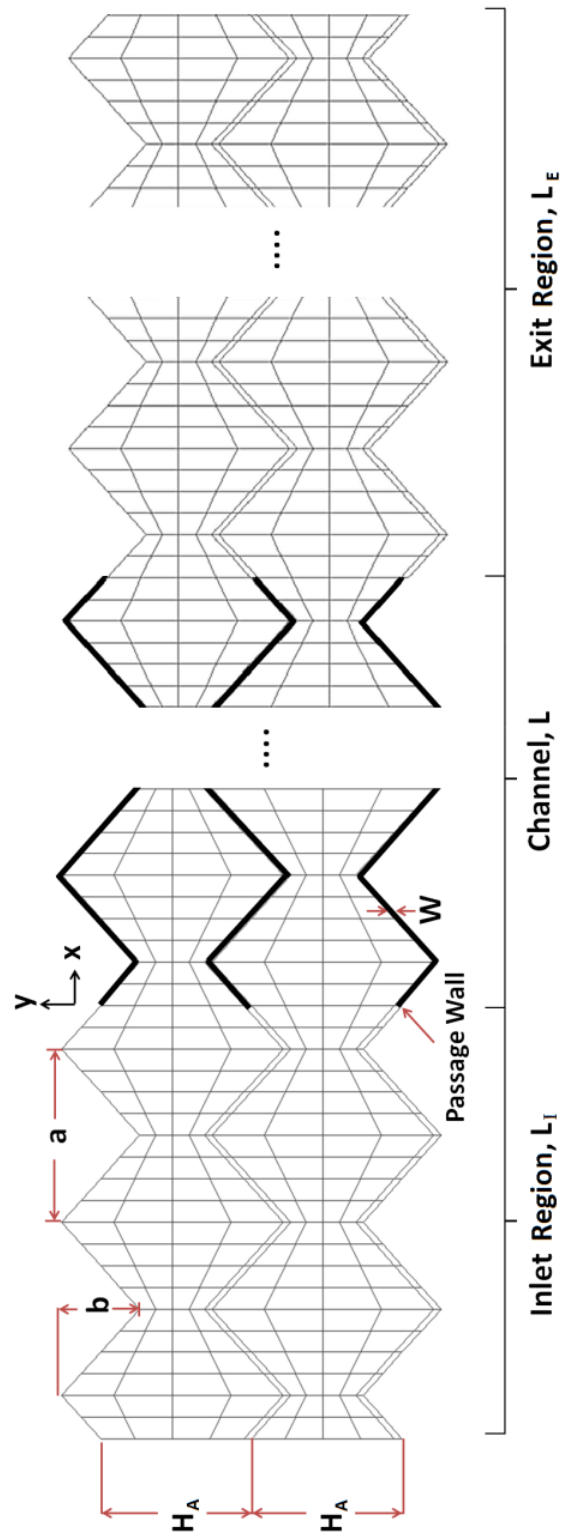


Figure 2-1. Computational domain and spectral element mesh.

In Figure 2-1, the groove depth normal the flow direction is b , length in the flow direction is a , the wall thickness in the y -direction is w , the average wall center-to-center spacing is H_A , and the minimum wall-to-wall spacing within the grooved channel is H_M . Previous studies used the ratio $a/H_M = 2.4$ since $\lambda = 2.4H_M$ is the most unstable Tollmien-Schlichting mode [13]. These previous studies also used a groove depth that is half the groove length so that the grooves act as open cavities [13]. The dimensionless geometric parameters for the current work are $a/H_M = 2.4$, $a/b = 2$, $w/H_A = 0.150$, $a/H_A = 0.925$, $b/H_A = 0.465$, and $H_M/H_A = 0.385$. In the current work, H_A is used to form the non-dimensional geometry groups in the passage. In the past, all dimensions were based on H_M .

Because of finite passage wall thickness, the cross section available for flow within the channels is smaller than that in the inlet and exit regions. Figure 2-1 shows that the upper passage begins in a converging portion of a groove, while the lower one starts with a diverging section. This configuration is used so that entrance heights for both upper and lower passages are the same. The passages are an integer number of groove lengths long (30), so Figure 2-1 shows the upper passage ending in a converging section while the lower ends with a diverging section.

The flow exits the domain using special outflow boundary conditions in the last vertical column of elements that avoids realization of reversed flow. The exit region is sufficiently long to allow the unsteady flow exiting from the grooved channel to decay to a steady flow before it exits the domain. This allows the pressure recovery that takes

place as the air decelerates (diffuses) outside the channel array to be calculated. This is important because it affects the total fan power that is required to propel the air through the passages.

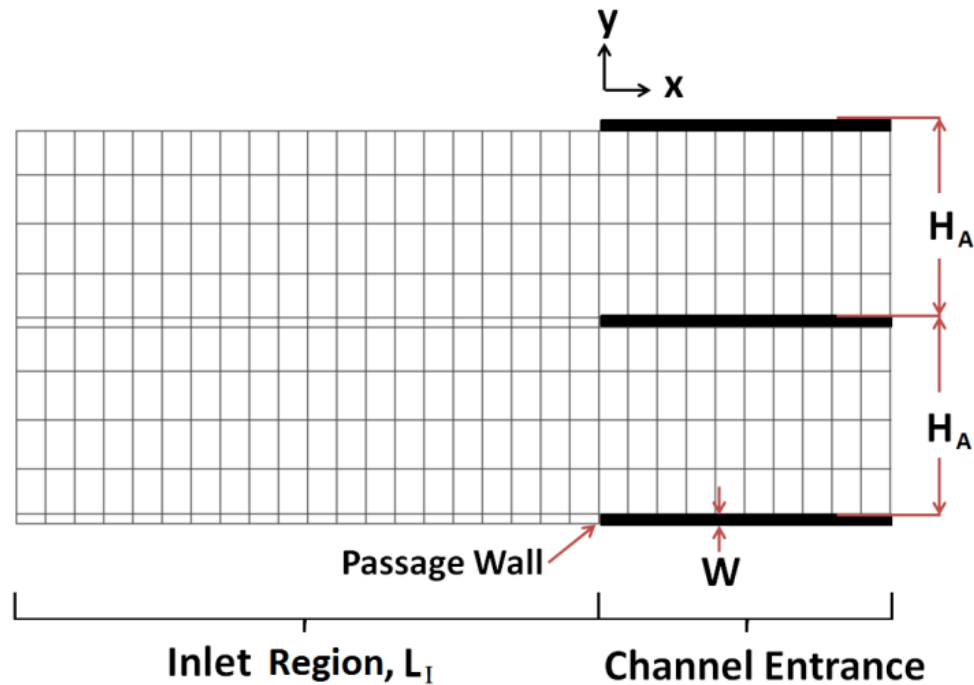


Figure 2-2. Spectral element mesh of inlet region and channel entrance for flat passage array.

Figure 2-2 shows the inlet region of a flat passage array used as a comparison with the grooved channel. The wall center-to-center spacing of these channels, H_A , is the same as the average wall center-to-center spacing of the grooved passage. The wall thickness in the y -direction, w , is also the same. The wall thickness normal to the wall surface is $\sqrt{2}$ times larger in the flat passage array compared with the grooved array. As a result, the volume of the walls for the two configurations is also the same. Because the

grooves are formed at a 45° , the surface area of the grooved channel is $\sqrt{2}$ times larger than that of the flat passage.

2.2 Spectral Element Method

In the spectral element method, the velocity, data, and geometry are expressed as tensor-product polynomials of degree N in each of K quadrilateral spectral elements, corresponding to a total grid point count of roughly KN^2 [27]. Numerical convergence is achieved by increasing the spectral order N . The present calculations were carried out at a base resolution of $K = 4120$, $N = 7$ (Figure 2-1 shows some spectral elements but not the KN^2 grid points). Resolution tests were performed for $Re = 1000$ and $Re = 3000$ at $N = 7$ and $N = 11$. The present simulations use consistent approximation spaces for velocity and pressure [28]. The momentum and pressure equations are advanced by first computing the convection term, followed by a linear Stokes Helmholtz and Poisson solve for the velocity and pressure terms, correspondingly. The characteristics-based operator-integration-factor splitting scheme used allows for Courant-Fredrichs-Lewy number as large as 2.5 while maintaining third-order accuracy in time. Full details of the method can be found in [27-31].

Direct numerical simulations were performed using the Nek5000 DNS/LES computational fluid dynamics solver developed at the Mathematics and Computer Science Division at Argonne National Laboratory [32].

2.3 Numerical Investigation

In this work, the hydraulic diameter is defined as follows.

$$D_H = \frac{4V}{A_p} = \frac{4L(2H_A)}{4L} = 2H_A \quad (1)$$

Here, V is the passage volume and A_p is the projected wetted area. In this work, the hydraulic diameter is twice the average wall center-to-center spacing. In previous studies, the hydraulic diameter was defined using the minimum wall-to-wall spacing. The use of the average wall center-to-center spacing offers a direct comparison to flat passage arrays.

The Reynolds number is defined as follows.

$$Re = \frac{u_0(2H_A)}{\nu} = \frac{2}{\nu} \int_B^T u \, dy \quad (2)$$

Here, ν is the fluid kinematic viscosity, and u is the axial (x -direction) component of the velocity. The integration is performed at a given x -location, from the bottom (B) to the top (T) of the domain. Since the flow rate is steady and the fluid is modeled to be incompressible, the integral is the same at all axial locations x and times t even though the flow is unsteady.

The investigation focused on the Reynolds numbers 1000, 1600, 2200, 2500 and 3000. The simulations analyzed both the grooved and flat passage arrays.

2.4 Onset of Oscillatory Flow

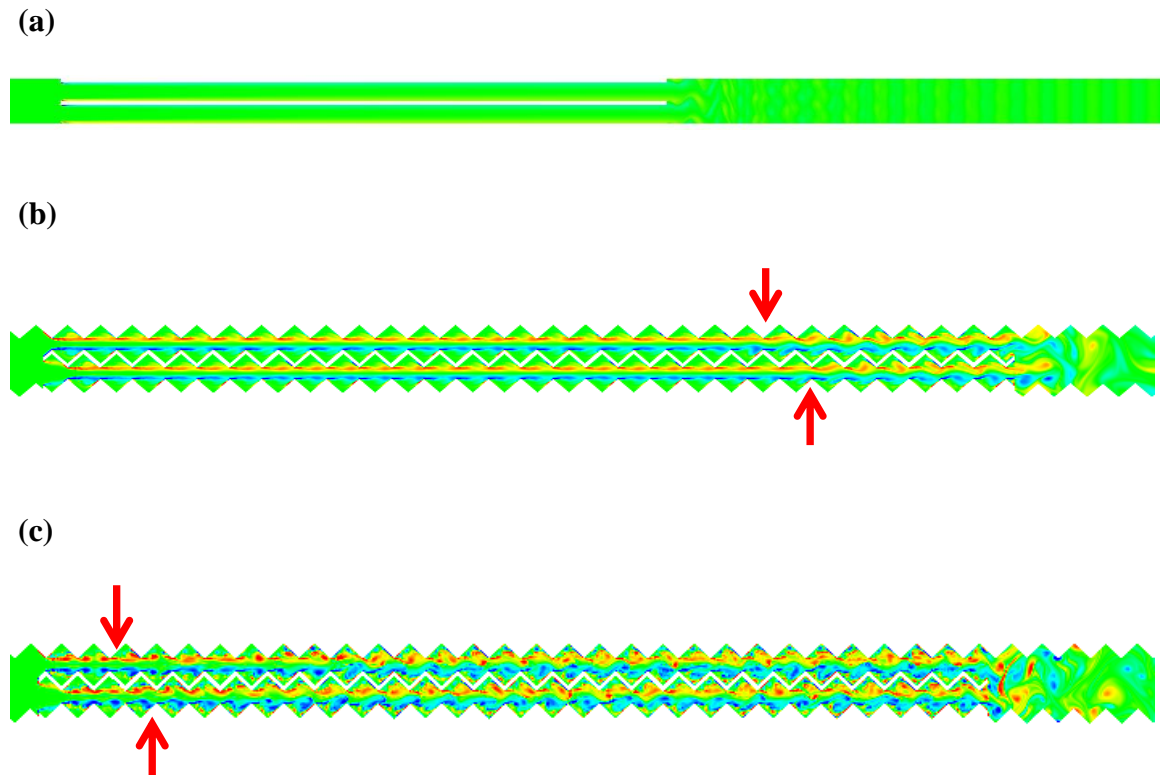


Figure 2-3. Fluid vorticity contour plots: (a) full domain flat passage at $Re = 3000$; (b) channel array at $Re = 1000$; (c) channel array at $Re = 3000$.

Figure 2-3 shows snapshots of contour plots of fluid vorticity after the flow has reached steady-state conditions. The plots are intended to help visualize the flow field. Figure 2-3a shows the entire computational domain for a flat passage array at $Re = 3000$. Figures 2-3b and 2-3c focus only on the grooved channel arrays (excluding most of the exit region) at $Re = 1000$ and 3000 , respectively.

In the flat passages, the vorticity contours are essentially parallel with the walls for all Reynolds numbers, indicating the flow is essentially parallel to the walls and is

steady. However, the current two-dimensional simulations cannot model the three-dimensional instabilities that may be present in flat passages at $Re > 2800$ [33].

Figure 2-3b shows that at $Re = 1000$, unsteadiness appears near the end of the grooved channels, roughly 24 groove lengths from the entrance ($x = 24a$) in the upper channel and 26 groove lengths from the entrance ($x = 26a$) in the lower channel. Figure 3c shows that at $Re = 3000$, unsteadiness appears near the channel entrance, roughly two groove lengths from the entrance in the upper channel and three groove lengths from the entrance in the lower channel. Arrows indicate these locations in Figures 2-3b and 2-3c. A similar analysis was performed at each Reynolds number investigated for both grooved and flat passage models. This onset location of oscillatory flow is different in each channel for four out of five Reynolds numbers investigated and moves upstream with an increasing Reynolds number. This difference in the onset location of oscillatory flow between the upper and lower channel could be due to the difference in inlet geometry. Further analysis is required to study the effect of inlet geometry on the onset location of oscillatory flow. Future work may include a more qualitative method for assessing the oscillatory onset location, such as plotting the root-mean-square velocity with location.

The solid diamonds in Figure 2-4 show the observed onset location of oscillatory flow versus x/D_H for the current simulations based on the vorticity contour plots. Horizontal error bars indicate the difference in onset location between the upper and lower channels. These onset locations are highly qualitative and were determined based the observed change in fluid stream from steady to oscillatory. Only the simulation at $Re = 2200$ had the same axial onset location for the upper and lower channels. The

onset location moves upstream with an increase in Reynolds number. For comparison, the onset location determined from experimental flow visualization data from a passage with one grooved and one flat wall is included from Greiner et al. 1990 [4]. The numerical results agree with experimental data at $Re = 1000$. The experimental data also show that the onset location moves upstream with increasing Reynolds numbers. For $Re > 1000$, the experimental onset locations are further upstream than those from the current simulations. The level of unsteadiness entering the experimental apparatus was not measured and may have had an effect on the onset location of oscillatory flow, whereas the unsteadiness entering the simulated channel is essentially non-existent.

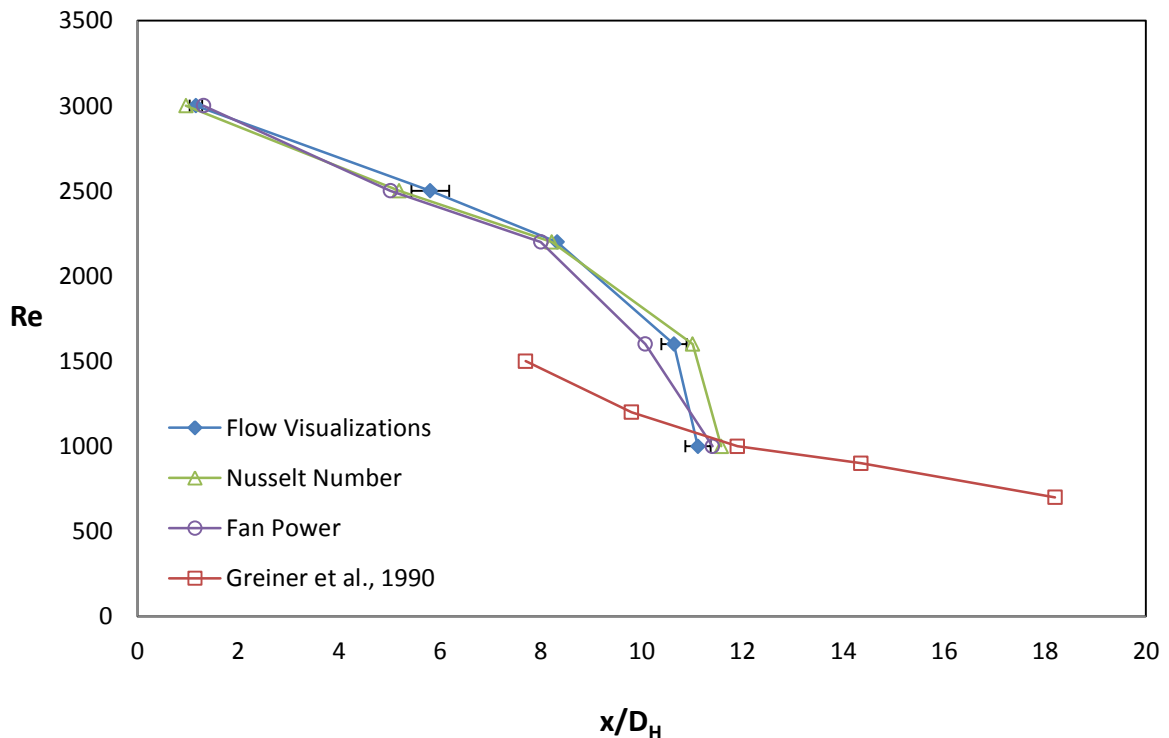


Figure 2-4. Observed onset location of oscillatory flow.

2.5 Heat Transfer Performance

In this work the average Nusselt number for a region between the inlet of the channel array ($x = 0$) and axial location x is defined as follows.

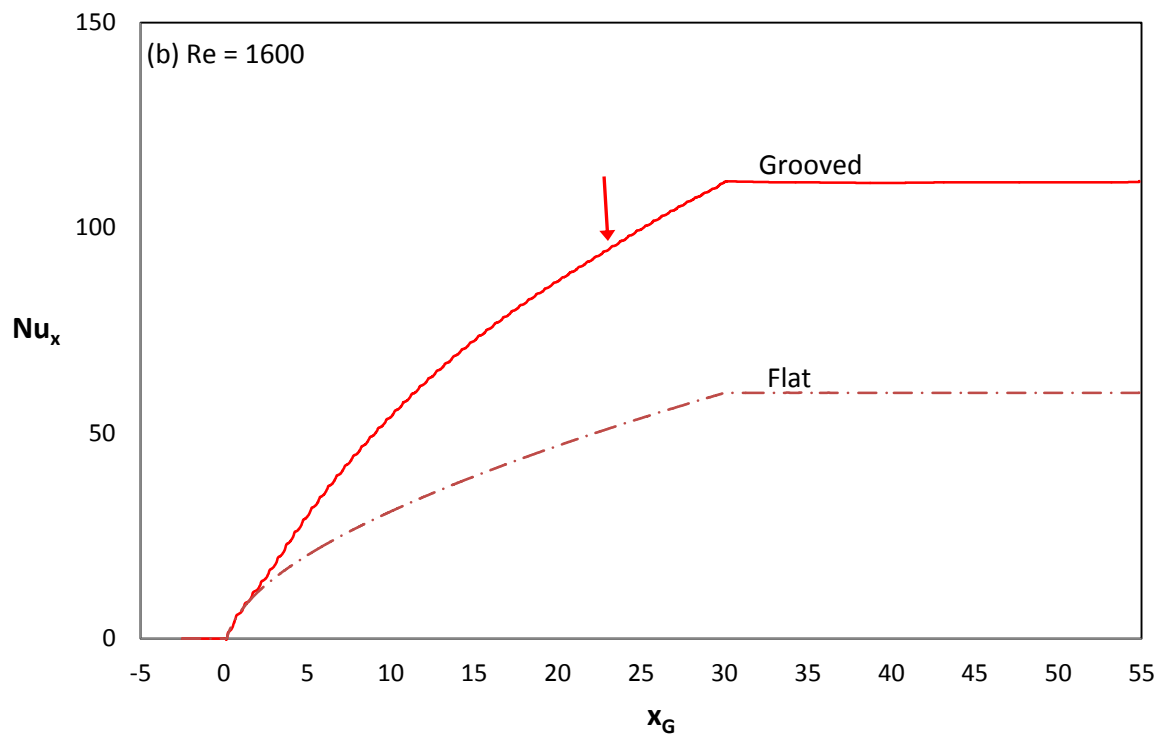
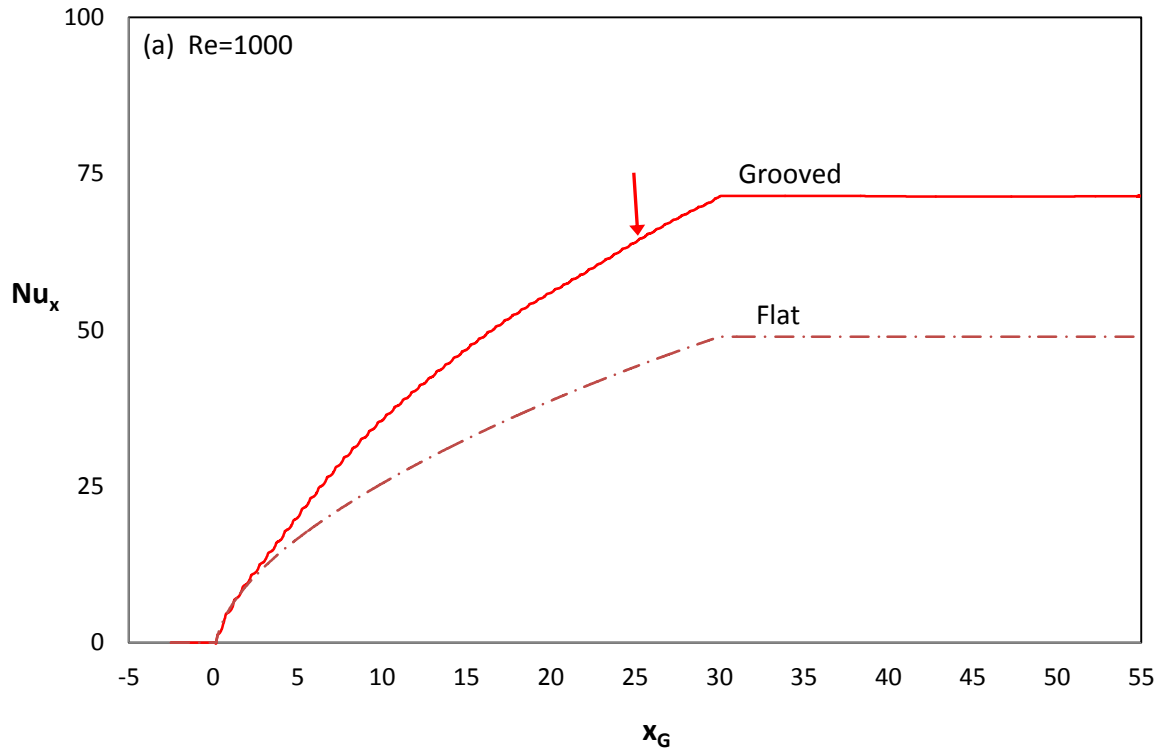
$$\begin{aligned}
 Nu_x &= \frac{h_x x}{k} = \frac{\bar{Q}(x)}{A_{px}(T_w - T_0)} \frac{x}{k} = \frac{\rho c_p \int_B^T (\bar{uT})_x dy}{4x(T_w - T_0)} \frac{x}{k} \\
 &= \frac{\int_B^T (\bar{uT})_x dy}{4\alpha}
 \end{aligned} \tag{3}$$

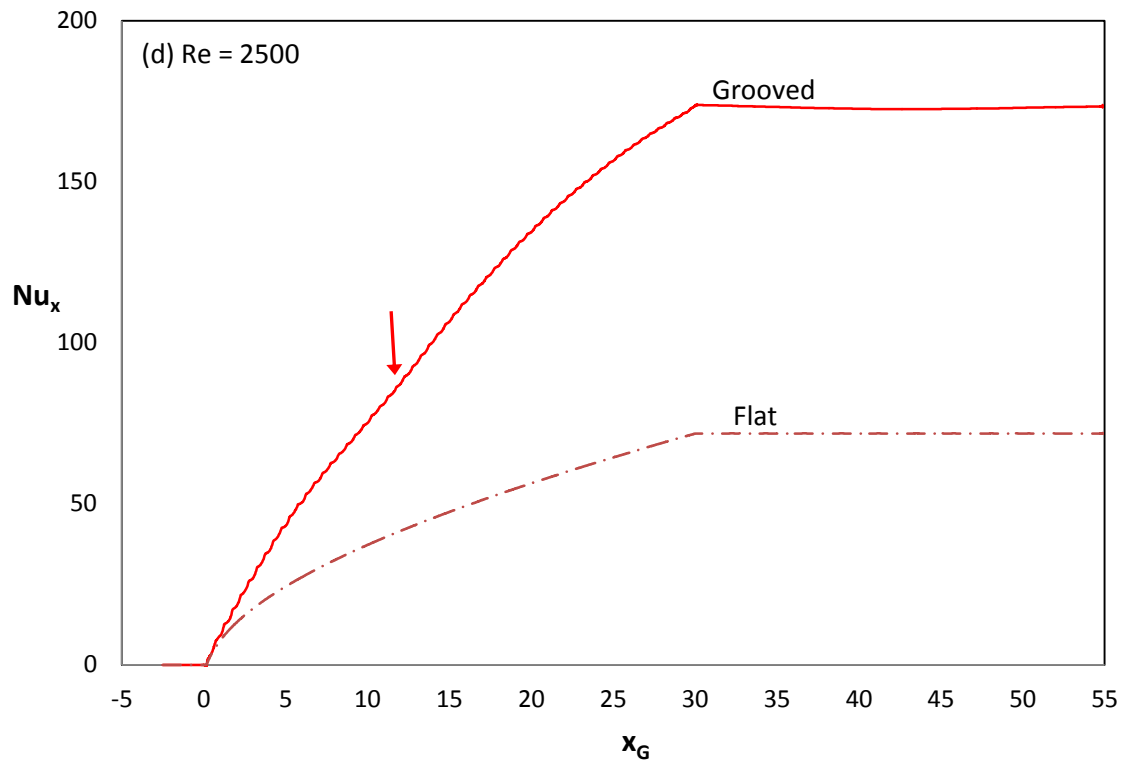
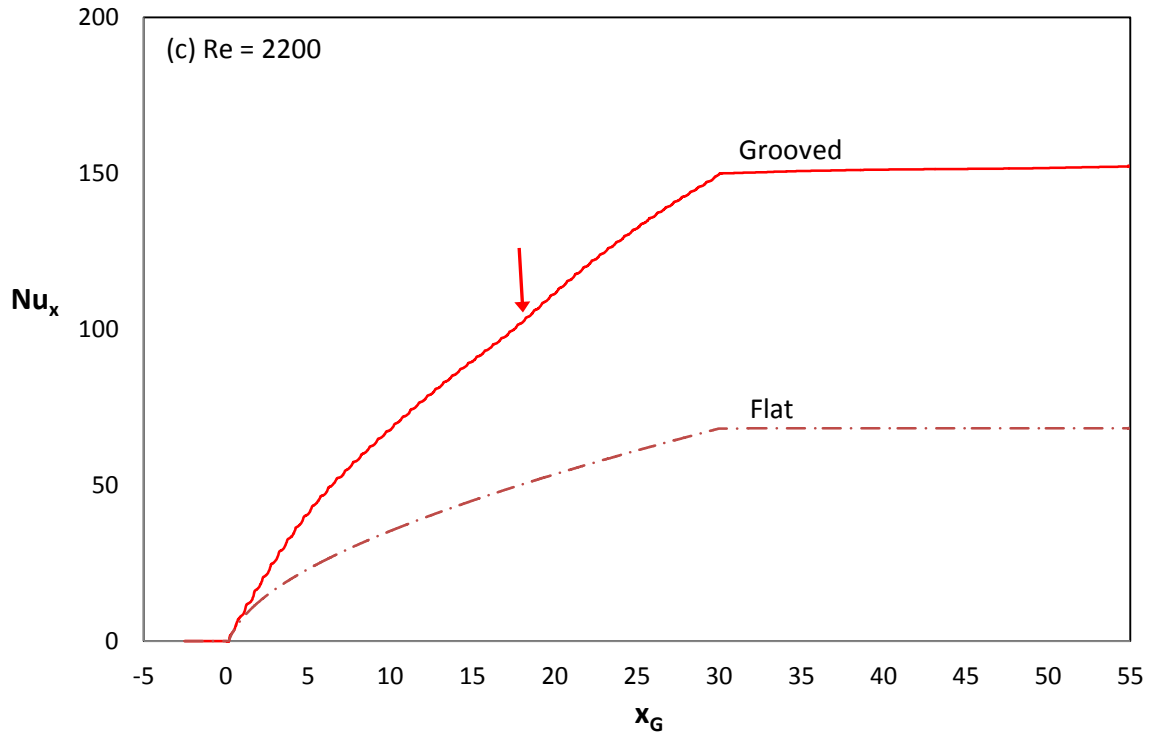
The over bar $\bar{\quad}$ denotes an average over time after the system has reached steady state, and the subscript $(\quad)_x$ indicates a value at the axial location x . In this expression, $\bar{Q}(x)$ is the total heat transfer from all four walls to the fluid from between the entrance to axial location x , $A_{px} = 4x$ is the total *projected* surface area for both walls of the two passages from the entrance to axial location x , and the temperature difference between the inlet gas and uniform temperature walls is $T_w - T_0 = 1 - 0 = 1$. Both $\bar{Q}(x)$ and $A_{px} = 4x$ are per unit length normal to the plane of figure 2-1. The fluid specific heat, density, thermal conductivity and thermal diffusivity are, respectively, c_p , ρ , k and $\alpha = k/\rho c_p$. While the simulation is running, Nu_x is calculated at every axial location x , which is dependent on the number of elements in x -direction and the polynomial degree, for each time step. The simulation is determined to have reached steady-state conditions after the bulk temperature in the exit region has reached a constant value. Once this steady-state condition is met, the Nusselt number data is time-averaged over a range of time steps

much greater than the period of the oscillations. This value quantifies the heat transfer from the inlet to an axial location x regardless of the shape of the walls.

Figure 2-5 shows the average Nusselt number, Nu_x , versus groove coordinate, $x_G = x/a$, for each Reynolds numbers investigated. Each plot includes the average Nusselt number for both the grooved and flat passage models. Solid lines are used for the grooved channel heat transfer, while dashed lines are used for the flat passage results.

Nu_x increases with x_G within the channel arrays because heat is transferred to the fluid in that region and the fluid temperature increases. It does not change upstream or downstream of the channels because there is no heat transfer outside of the channels. For the flat passage arrays, the slope of the average Nusselt number decreases as the distance from the channel inlet increases. This rate of decrease is caused by the growth of the boundary layer. For the grooved passage arrays, the rate of decrease is less than that for the flat passages. Near the channel entrance, Nu_x is the same for both grooved and flat models but diverges after several groove lengths. This divergence location moves nearer the channel entrance with an increase in Reynolds number, similar to the behavior of the instability onset location. A slight change in curvature can be seen in the Nu_x versus x_G plots for grooved passages at all Reynolds numbers. The locations of these changes are indicated by arrows. The location of the change in curvature is plotted versus x/D_H in Figure 2-4 using open triangles. At each Reynolds number, this location is very close to the onset of unsteady flow locations described earlier (diamonds in Figure 2-4). This suggests that the slight curvature changes are caused by the onset of unsteady flow.





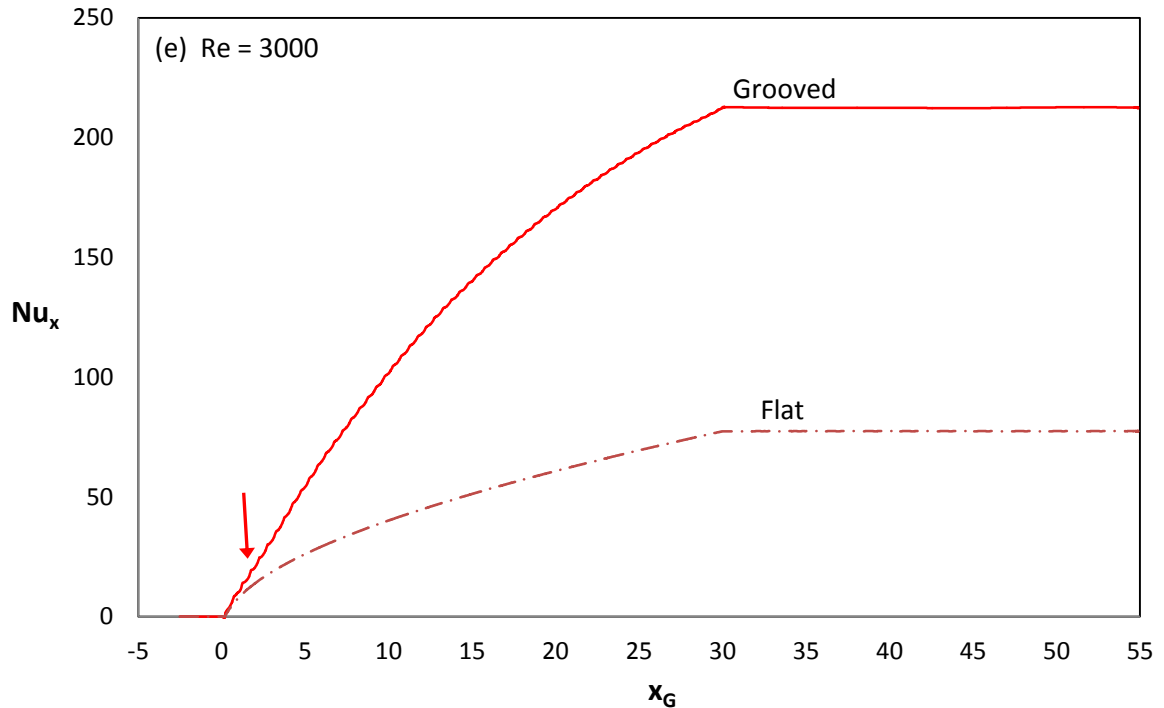


Figure 2-5. Average Nusselt number versus groove coordinate (a) $Re = 1000$; (b) $Re = 1600$; (c) $Re = 2200$; (d) $Re = 2500$; (e) $Re = 3000$

A resolution test was performed at Reynolds numbers of 1000 and 3000 to determine whether or not the solution is grid-independent. The polynomial degree was increased from $N = 7$ to $N = 11$. By increasing the polynomial degree, the number of grid points increased from 201,880 to 498,520. Figure 2-6 shows the grooved passage average Nusselt number for both lower ($N = 7$) and higher ($N = 11$) resolution grids. For both $Re = 1000$ and 3000, the $N = 7$ (solid red) and $N = 11$ (dashed green) results are nearly identical, indicating that the results are essentially grid independent.

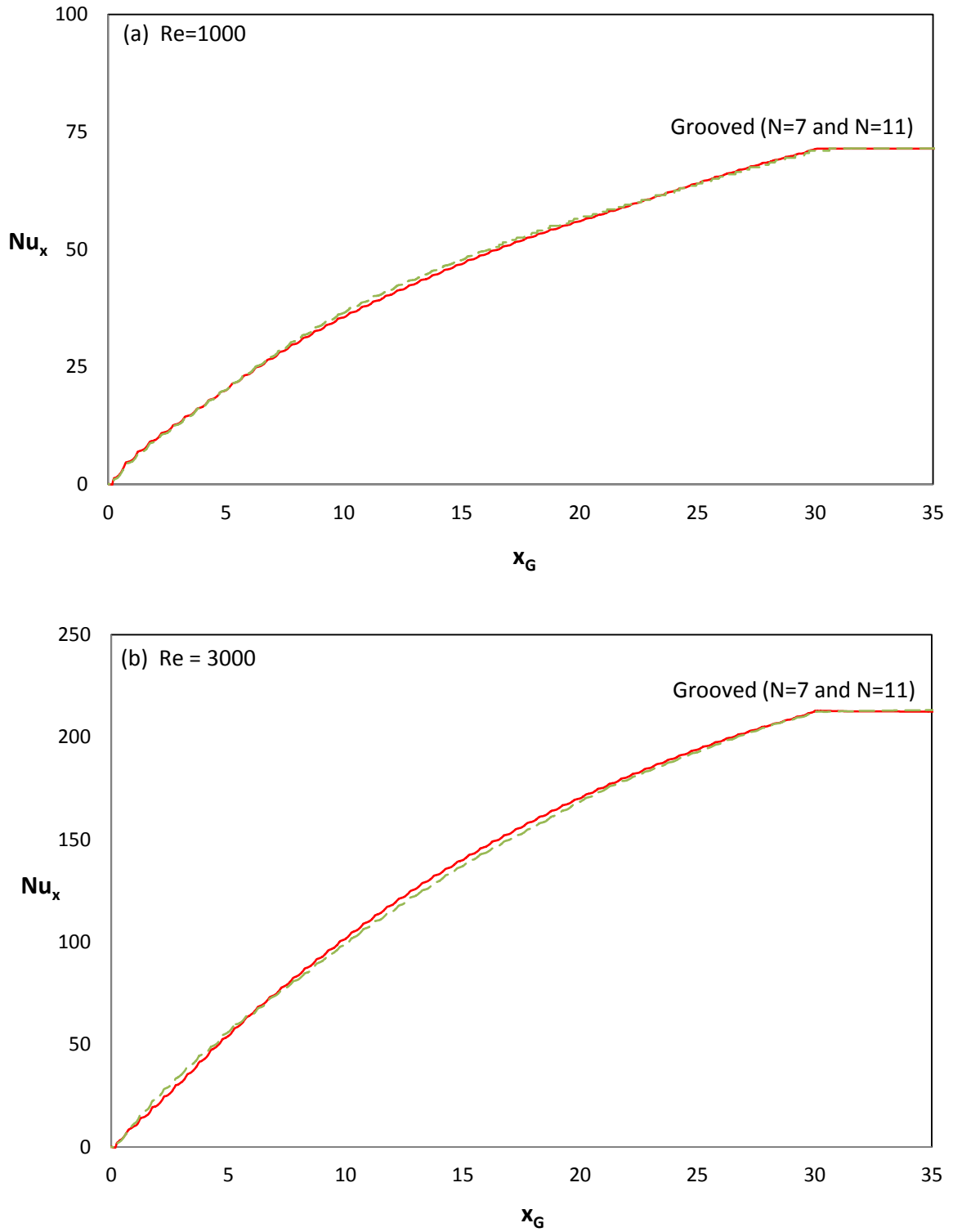


Figure 2-6. Average Nusselt number resolution test: (a) $Re = 1000$; (b) $Re = 3000$.

The full channel average Nusselt number, Nu_L , is the value of Nu_x at $x_G = 30$, and it characterizes the total heat transfer to the air from the array walls. Figure 2-7 shows the full channel average Nusselt number for both the grooved passages, $Nu_{L,G}$, and flat passages, $Nu_{L,F}$, versus Reynolds number. The heat transfer enhancement for a grooved array over a flat array increases with Reynolds number from a ratio of 1.46 at $Re = 1000$ to a ratio of 2.75 at $Re = 3000$. The dashed line marked $\sqrt{2} Nu_{L,F}$ shows the level of enhanced heat transfer that would be expected due to the area increase alone. It can be seen that most all of the enhancement is due to area increase at $Re = 1000$, and this is consistent with the onset of unsteady flow being near the channel exit at that Reynolds number (Figure 2-3b). Figure 2-7 shows that enhancement due to flow unsteadiness and convective transport increases for Reynolds numbers greater than 1000. At Reynolds numbers lower than those investigated in the current work, the total average Nusselt number for the grooved passage arrays would likely be lower than that of $\sqrt{2} Nu_{L,F}$ for the same Reynolds number because the flow can become stagnant in the open cavities that the grooves form. Figure 2-7 also includes the data from the $N = 11$ simulations at $Re = 1000$ and 3000. These are represented by open circles, and the values are nearly equal to the $N = 7$ results.

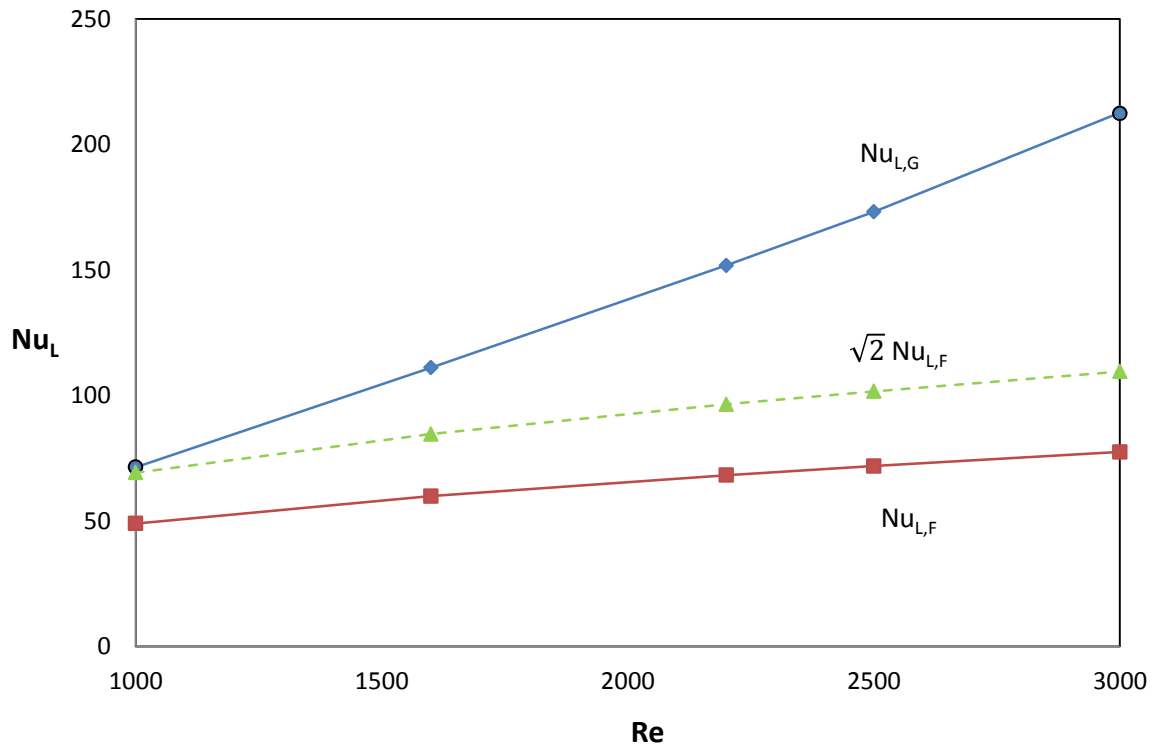


Figure 2-7. Average full channel Nusselt number versus Reynolds number.

2.6 Pressure Drop Analysis

The solid blue line in Figure 2-9 shows the pressure drop results for the spectral element simulation of a flat passage array at $Re = 1000$. Since the flow is steady and incompressible in the flat passage array at that Reynolds number, the pressure does not change with time. Pressure was taken along the centerline of each passage (upper and lower) at an instant in time after the simulation had reached steady-state conditions. The pressure was analyzed at different y -locations within the array, and it was determined that pressure does not vary with y . The results show a large initial pressure drop as flow accelerates into the array. There is a steady increase in pressure drop due to core friction

within the array and then the pressure drop decreases to a constant value in the exit region.

Kays and London define the core pressure drop for an array of parallel-wall passages as follows [34].

$$\Delta P = \frac{G^2}{2} v_1 \left[(K_c + 1 - \sigma^2) + 2 \left(\frac{v_1}{v_2} - 1 \right) + f \frac{A}{A_c} \frac{v_m}{v_1} - (1 - \sigma^2 - K_e) \frac{v_2}{v_1} \right] \quad (4)$$

In this equation, ΔP is the pressure drop from inlet region to exit region, v is the velocity at locations shown on Figure 2-8, $G = \rho v$ is the mass velocity, σ is the ratio of free-flow area to frontal area, f is the mean friction factor, A is the exchanger total heat transfer area on the air side, A_c is the exchanger minimum free-flow area, and K_c and K_e are the entrance and exit loss coefficients, respectively. For the current analysis, the gravitational effects are negligible, and the mean velocity defined as follows.

$$v_m \approx \frac{v_1 + v_2}{2} \quad (5)$$

This mean velocity is assumed to be equal to the velocity in the inlet plenum since the density is assumed constant. The first term in equation (4), $(K_c + 1 - \sigma^2)$, describes the entrance effect. The second term, $2 \left(\frac{v_1}{v_2} - 1 \right)$, describes the flow acceleration. The third term, $f \frac{A}{A_c} \frac{v_m}{v_1}$, describes the core friction within the array. The fourth and final term, $(1 - \sigma^2 - K_e) \frac{v_2}{v_1}$, describes the exit effect.

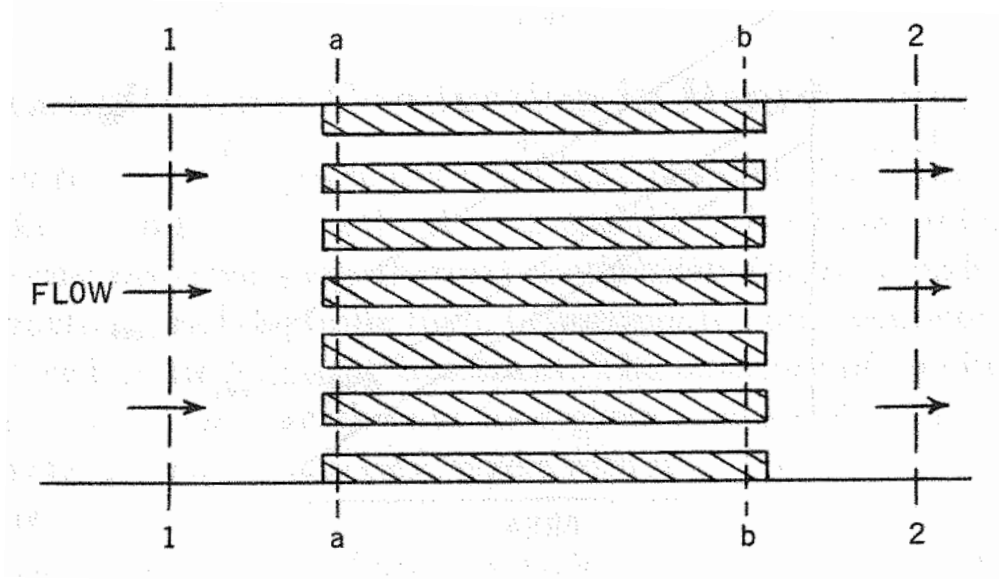


Figure 2-8. Heat exchanger core model for pressure-drop analysis from Kays and London [34].

The mean friction factor was calculated using Shah's correlation for flow in the inlet of ducts, which is valid within ± 2 percent for many duct shapes [35].

$$C_{f,app}Re = \frac{3.44}{\sqrt{\zeta}} + \frac{C_{fp}Re + K_{\infty}/4\zeta - 3.44/\sqrt{\zeta}}{1 + c/\zeta^2} \quad (6)$$

This equations correlates with a Graetz-type variable defined as follows.

$$\zeta = (x/D)/Re_D \quad (7)$$

For parallel-wall ducts, $C_{fp}Re = 24$, $K_{\infty} = 0.674$, and $c = 0.000029$ [35].

Using equations (4) through (7), the pressure drop was calculated for a parallel-wall duct with the same geometry as the flat passage array model and for a Reynolds number of 1000 and plotted alongside the numerical result in Figure 2-9 (marked with

triangles). The correlation for the first term of equation (4) results in a greater pressure drop at the array inlet than the simulated results. The core pressure drop calculated from equation (6) is a function of the distance from the array inlet, and the maximum pressure drop at the channel exit is approximately the same for both the calculation and the simulation. The total pressure drop from the inlet region to the exit region is also approximately the same for both the analytic and simulated solutions. This indicates that the two-dimensional simulation is accurate for laminar flows in flat passage arrays. However, only one of the investigated Reynolds numbers was analyzed. Future work should perform a similar study on all considered Reynolds numbers.

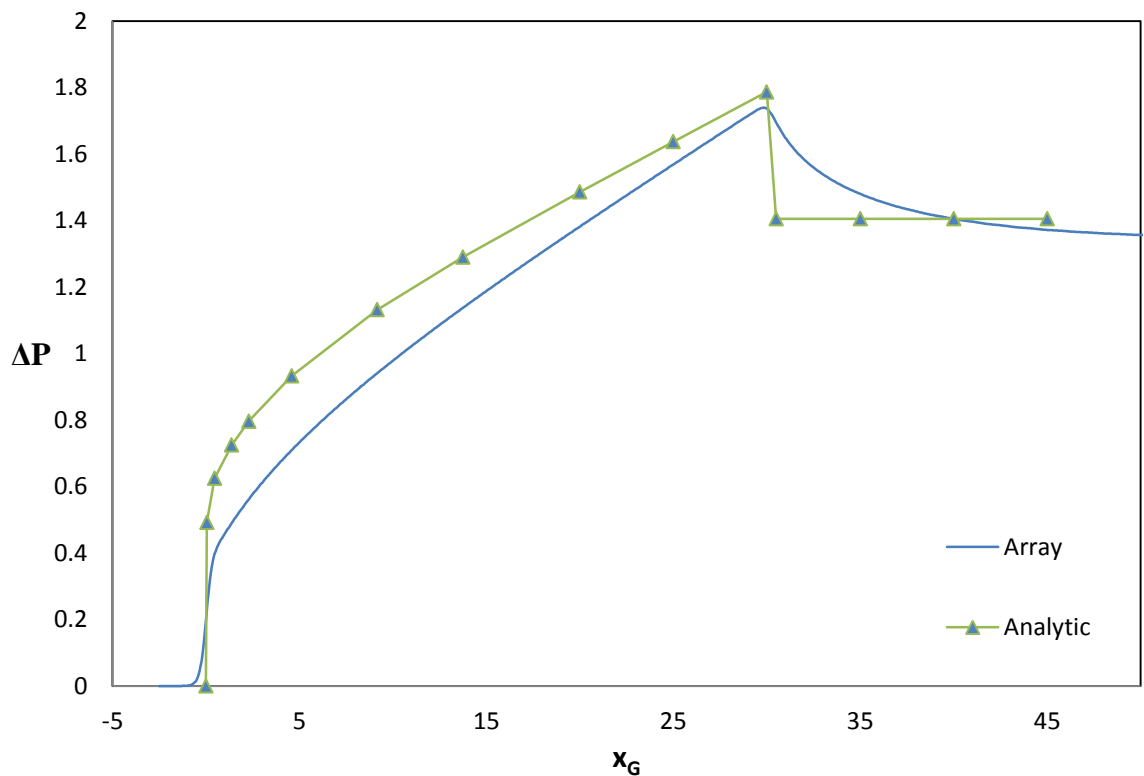


Figure 2-9. Non-dimensional pressure drop for $Re = 1000$

2.7 Fan Power Performance

Figure 2-10 shows a general open thermodynamic system with a non-uniform cross-section where matter may flow in and out of the system boundaries. Energy is required to move a fluid through the system from the inlet to the outlet.

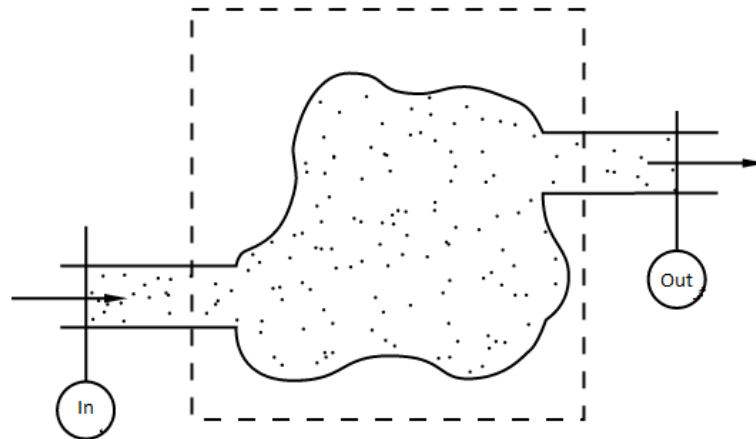


Figure 2-10. Open thermodynamic system.

The net rate required to move a fluid through the system is defined as follows.

$$\dot{W} = \int (Pv d\dot{m})_{in} - \int (Pv d\dot{m})_{out} \quad (8)$$

In this expression, \dot{W} is the net work rate for the system, P is the pressure, $v = 1/\rho$ is the specific volume, and $d\dot{m}$ is the mass flow rate and is defined as follows.

$$d\dot{m} = \rho v dA \quad (9)$$

After substituting equation (9) into equation (8) and cancelling out the density, the result is as follows.

$$\dot{W} = \int (PudA)_{in} - \int (PudA)_{out} \quad (10)$$

For a two-dimensional case, as in the current work, the integral over the area can be changed to a line integral over y . Furthermore, this rate can be time-averaged to yield a total work required to move a fluid from the inlet, through the system, to the outlet. This final result is as follows.

$$W = \int (\overline{Pu})_{in} dy - \int (\overline{Pu})_{out} dy \quad (11)$$

Equation (11) has the units of power. This can be multiplied by $1/\rho u^2 v$ to form a dimensionless parameter. The non-dimensional fan power or power required to move the gas against drag in the channel from its entrance at $x = 0$ to another x -location is defined as follows.

$$\Phi_x = \frac{1}{\rho u_0^2 v} \left[\int_B^T (\overline{uP})_{x=0} dy - \int_B^T (\overline{uP})_x dy \right] \quad (12)$$

Φ_x is a volumetric flow rate average pressure drop between the pressure at $x = 0$ and axial location x . The dimensionless fan power is a tool used in combination with the average Nusselt number to design heat exchanger devices. As with the average Nusselt number calculation, the dimensionless fan power is calculated at each axial location x for every time step. Once the simulations have reached steady-state conditions, the dimensionless fan power is time-averaged over a number of time steps much greater than the period of the oscillations.

Figure 2-11 shows the non-dimensional fan power versus x_G for $Re = 1000$, 1600, 2200, 2500 and 3000 for both grooved and flat passages. On the scale of this plot,

the flat passage fan powers are very close to each other and only the upper ($Re = 3000$) and lower ($Re = 1000$) curves are marked. For all locations and Reynolds numbers the grooved passage flows require a significantly higher fan power than in the flat channel. For the grooved passage array at $Re = 3000$, the fan power exhibits a sharp increase at the channel entrance where the flow accelerates into the channel array. This acceleration is caused by blockage from the grooved wall's thickness and shape. The air must accelerate around this blockage as it enters the passage. Some of the pressure is recovered in the first few grooves as the velocity field becomes established following the *vena contracta*. Further downstream, the fan power continues to increase due to drag within the channels. The fan power within the channel array oscillates as the flow accelerates and decelerates in the converging and diverging sections of the channel. Since the grooves are offset between the upper and lower passage, there are twice as many oscillations than there are grooves. The fan power decreases as the flow decelerates into the exit region where the pressure increases. The fan power and pressure reach their final values at roughly $x_G = 45$, which is 15 groove lengths downstream of the channel exit.

At lower Reynolds numbers, the fan power exhibits a similar behavior with a sharp increase at the channel entrance, small recovery, increase due to drag within the channel array, and decrease in the exit region. However, at lower Reynolds numbers the amplitude of the oscillations and the overall slope are small in a region near the inlet. Further downstream, the amplitude and slope both increase significantly. This location is marked by an arrow for each Reynolds number, and these locations are shown as fan

power data points in Figure 2-4 (marked by open circles). These locations move upstream with an increase in Reynolds number and are in good agreement with the locations of the onset of flow unsteadiness and location where the Nusselt number exhibits a change in curvature. This suggests that the increase in amplitude and slope are caused by the onset of unsteady flow.

The flat passage fan power curves exhibit a slight increase in the flat passage arrays at the channel entrance and a slight decrease at the channel exit. These changes are much smaller than those of the grooved channels because the flat passage blockage is much smaller. Fan power is significantly greater in the grooved passage arrays than in the flat passage arrays.

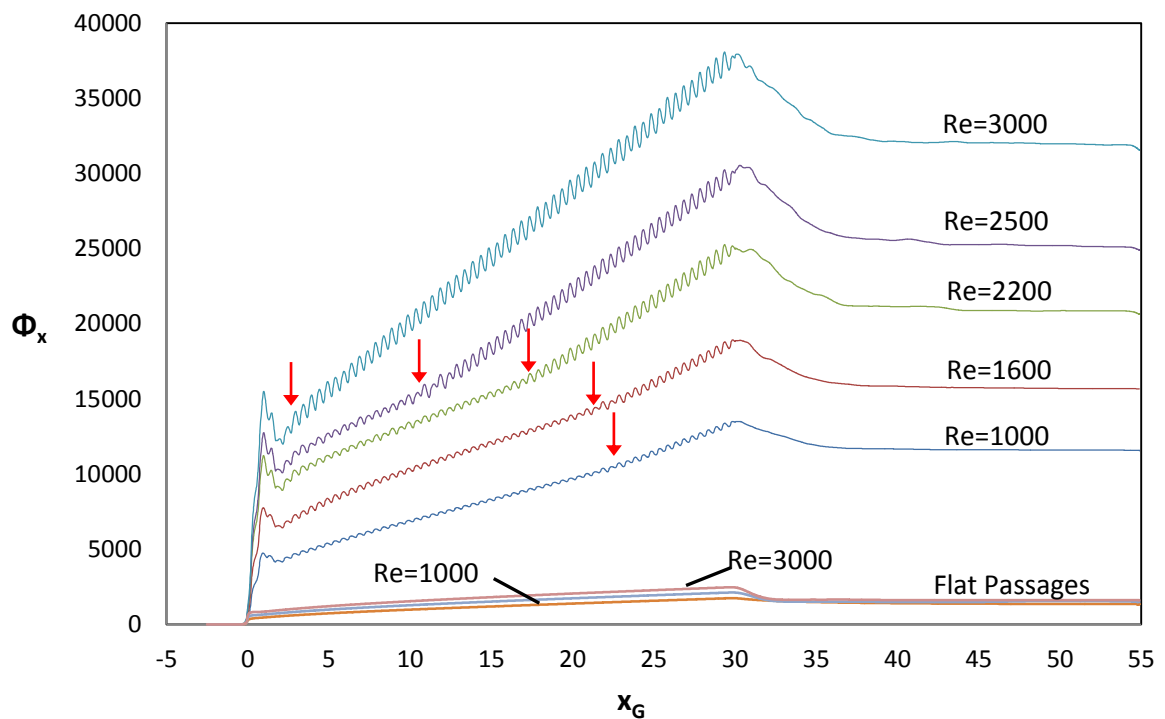


Figure 2-11. Non-dimensional fan power versus groove coordinate for Re = 1000, 1600, 2200, 2500 and 3000.

The fan power contribution from the grooved passage inlet and exit effects, Φ_{i-e} , can be defined as the fan power at the trough following the *vena contracta* minus the fan power recovery (the maximum fan power at the array exit minus the full channel fan power). This fan power contribution would likely be the same if the grooved passages were extended to an infinite length. The fan power contribution from within the grooved passage arrays, Φ_{chan} , can be defined as the maximum fan power at the array exit minus the fan power at the trough following the *vena contracta*. This contribution is dependent on the length of the grooved passage. Figure 2-12 shows both Φ_{i-e} and Φ_{chan} versus the Reynolds number for the grooved passages. For all Reynolds numbers investigated, Φ_{chan} is greater than Φ_{i-e} . Furthermore, both increase with an increase in Reynolds number. Figure 2-13 shows the fan power ratio, Φ_{ratio} , which is defined as Φ_{chan} divided by Φ_{i-e} . This value varies slightly between 3.5 and 4.5 for the Reynolds numbers investigated.

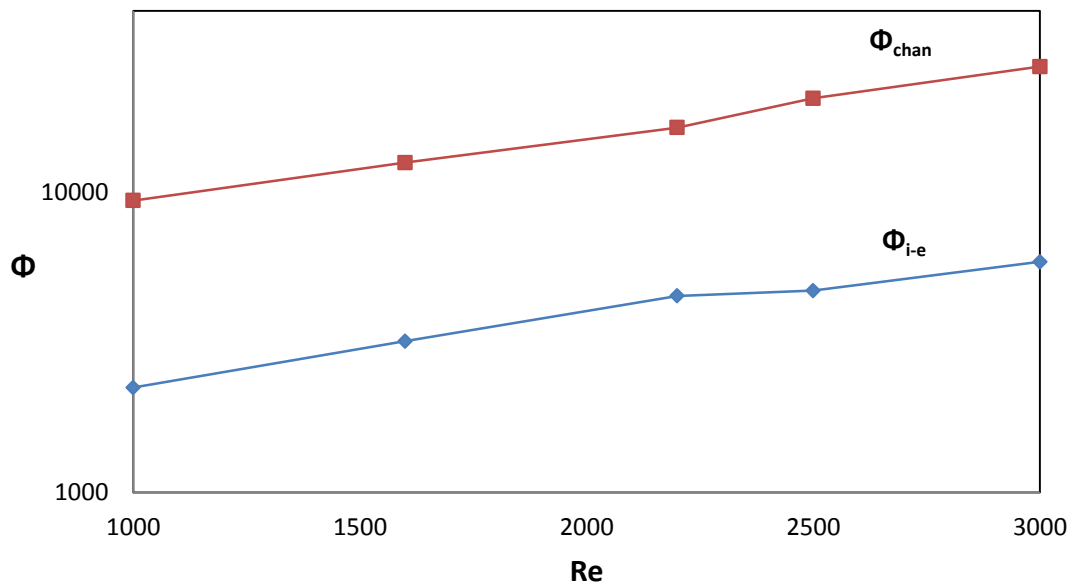


Figure 2-12. Fan power contributions versus Reynolds number.

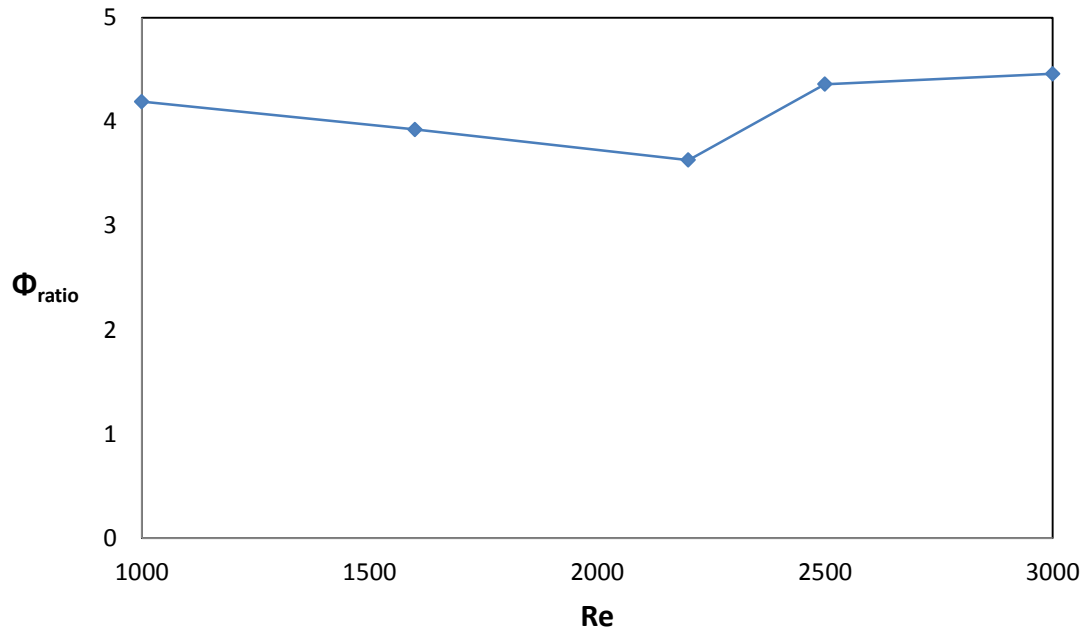


Figure 2-13. Fan power contribution ratio versus Reynolds number.

The full channel non-dimensional fan power, Φ_L , is the value of Φ_x at $x_G = 50$. It characterizes the total fan power required to accelerate the flow into the array, push the fluid through the array, and the recovery after it exits the array. Figure 2-14 shows Φ_L versus Reynolds number for grooved ($\Phi_{L,G}$) and flat ($\Phi_{L,F}$) arrays. For all Reynolds numbers, the fan power is significantly greater in the grooved passage arrays than in the flat passage arrays. The required fan power also increases more significantly with Reynolds number in the grooved passage arrays than in the flat passage arrays. The fan power requirement for a grooved array over a flat array increases with Reynolds number from a ratio of 8.56 at $Re = 1000$ to a ratio of 18.10 at $Re = 3000$. Figure 2-14 also includes the data from the $N = 11$ simulations at $Re = 1000$ and 3000 , represented by open circles. The values are nearly equal to the $N = 7$ results at $Re = 1000$, but slightly lower at $Re = 3000$.

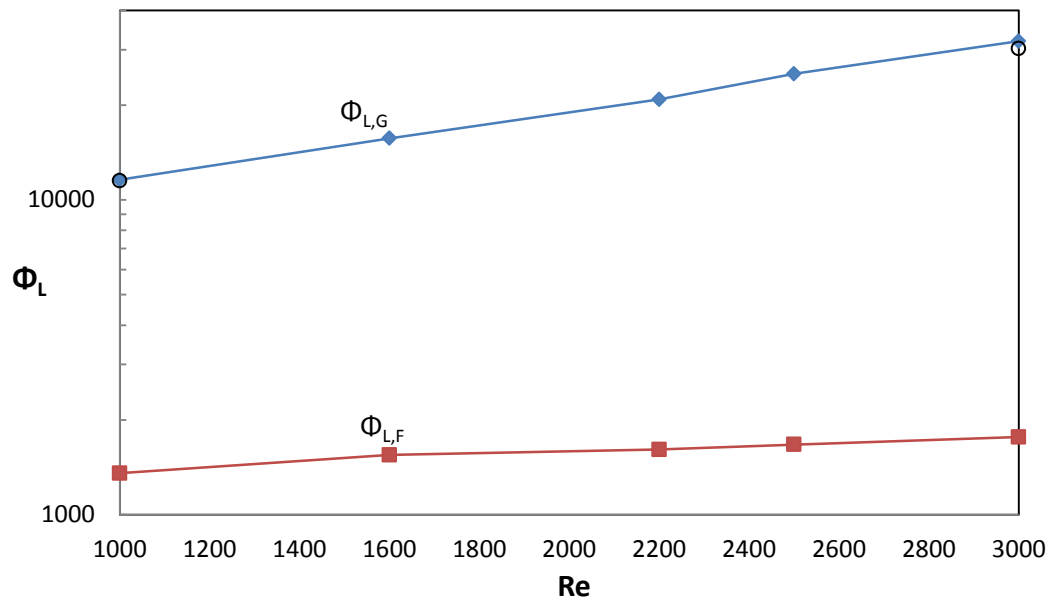


Figure 2-14. Full channel non-dimensional fan power versus Reynolds number.

Figure 2-15 shows Nu_L versus Φ_L for both grooved and flat passage arrays at $Re = 1000, 1600, 2200, 2500$ and 3000 . Heat transfer augmentation can be achieved by using grooved passage arrays but only with a significant increase in the required fan power. The flow in the grooved passage arrays likely become fully-developed before exiting the passages. The flow in the flat passage arrays, however, are still in developing regions. If the flat passages were extended to an infinite length, the flat passages curve in Figure 2-15 would become fully horizontal as was seen in previous experimental results [13].

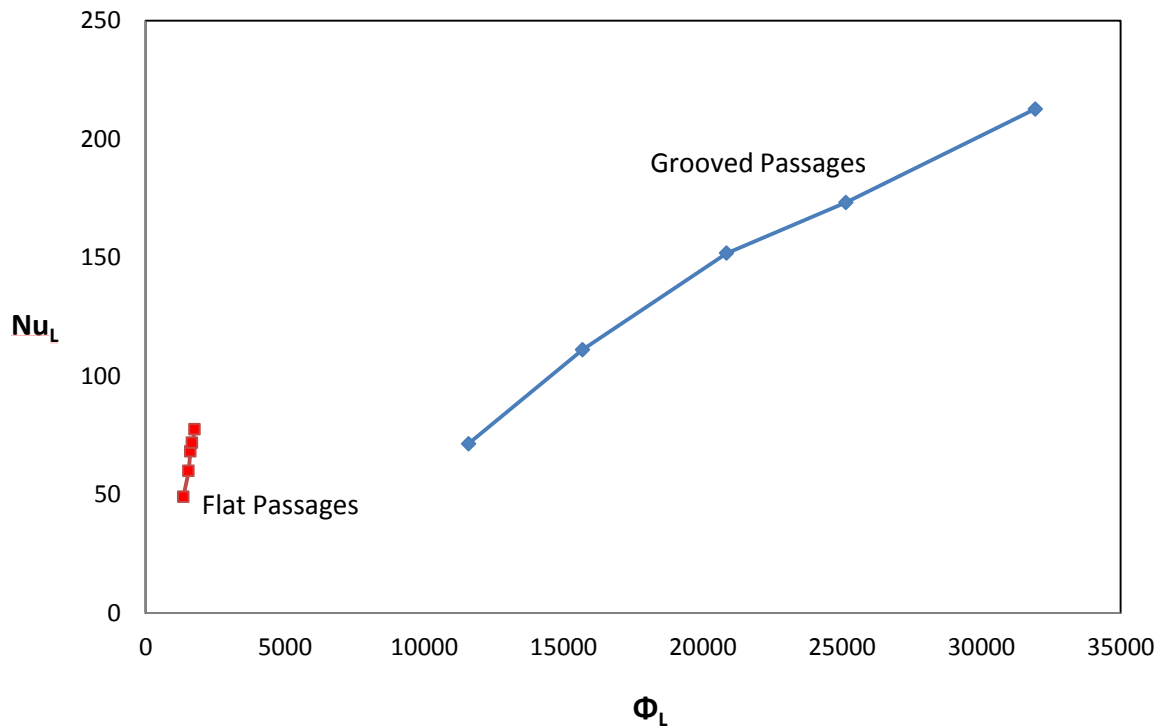


Figure 2-15. Full channel average Nusselt number versus full channel non-dimensional fan power.

2.8 Summary

Steady-state results show that the addition of transverse grooves to the parallel passage arrays introduces unsteadiness a number of grooves downstream of the channel entrance. This onset location moves closer to the channel entrance as the Reynolds number increases. Figure 2-16 shows the heat transfer enhancement ratio, χ_{Nu} , versus Reynolds number. χ_{Nu} is defined as the grooved passage total average Nusselt number normalized by the flat passage total average Nusselt number.

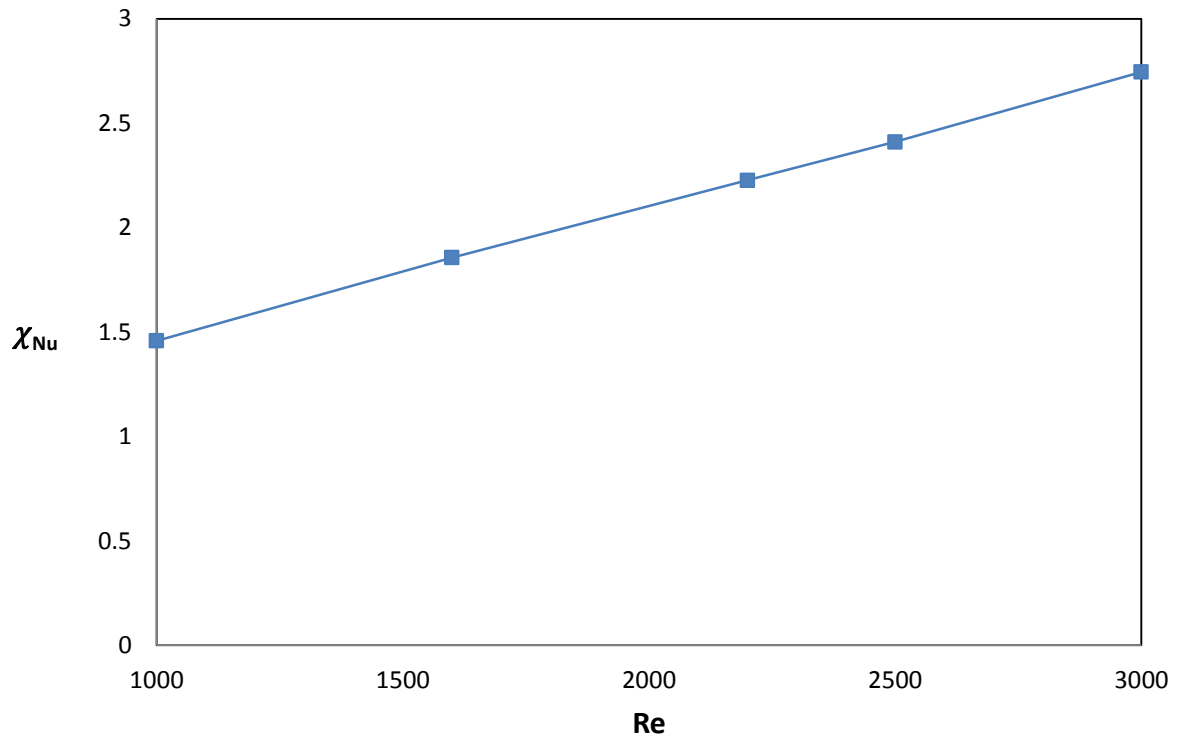


Figure 2-16. Heat transfer enhancement ratio versus Reynolds number.

Similarly, the fan power requirement ratio, χ_{FP} , is defined as the grooved passage total dimensionless fan power normalized by the flat passage total dimensionless fan power. Figure 2-17 shows the fan power requirement ratio versus Reynolds number.

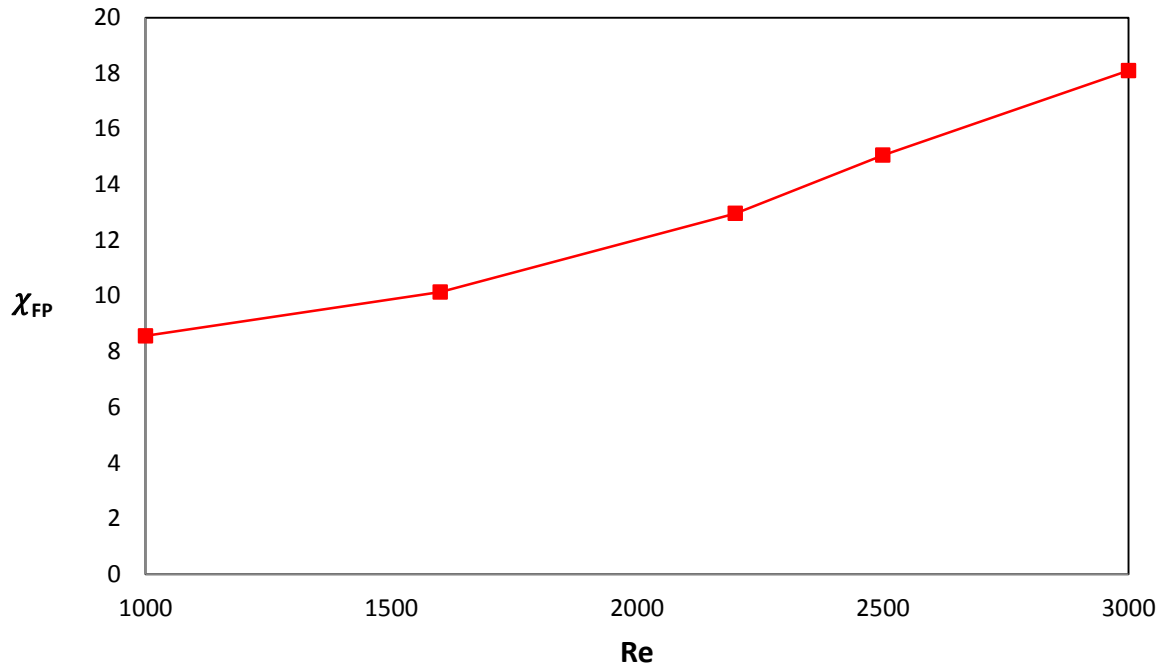


Figure 2-17. Fan power requirement ratio versus Reynolds number.

Figure 2-16 shows that unsteadiness improves the overall heat transfer compared with a flat passage array of equal average channel height by a factor of 1.46 at $Re = 1000$ and a factor of 2.75 at $Re = 3000$. Figure 2-17 shows that grooves also cause an increase in the required fan power by a factor of 8.56 at $Re = 1000$ and by a factor of 18.10 at $Re = 3000$. However, these two-dimensional results may not adequately capture the entire instability and mixing structures that have been seen in experiments and three-dimensional simulations. These simulations have provided preliminary results about developing flow in grooved passage arrays in a relatively short amount of time compared to three-dimensional simulations. The next step is to develop a three-dimensional model with simplified inlet and exit conditions to study developing flow and then consider the full inlet and exit effects.

Chapter 3: Two-Dimensional Single Channel

3.1 Domain Design

Due to the large size of the two-dimensional model described in Chapter 2, it was determined that a smaller domain should be used to analyze developing flow in a passage with transverse surface grooves in three dimensions. However, prior to developing a three-dimensional, single channel mesh, a two-dimensional, single channel mesh was designed to be compared with the two-dimensional array models. Figure 3-1 shows the two-dimensional, single channel mesh that was used as a comparison to the array model. Flow with a Prandtl number of 0.7 (air) enters the left side of an inlet plenum shorter than in the array model ($L_I = 0.6a$) and then encounters a single grooved channel. The channel entrance height is the maximum flow area, $H_M + 2b$, so that periodic boundary conditions could be applied to the upper and lower edges of the inlet and exit regions. The channel has a finite wall thickness, $w = 0.150H_A$. The length of the channel is $L = 30 a$ and the dimensionless groups defining the groove dimensions are the same as with the array model. Because there are an integer number of grooves, the channel begins with a converging section and ends with a diverging section. The flow exits the channel into an exit region ($L_E = 14.8a$) where flow unsteadiness decays to steady flow before exiting the domain using the same special outflow conditions as was used in the array model. There are 896 elements in the single channel model as compared to the 4120 in the array model. The polynomial degree is $N = 7$.

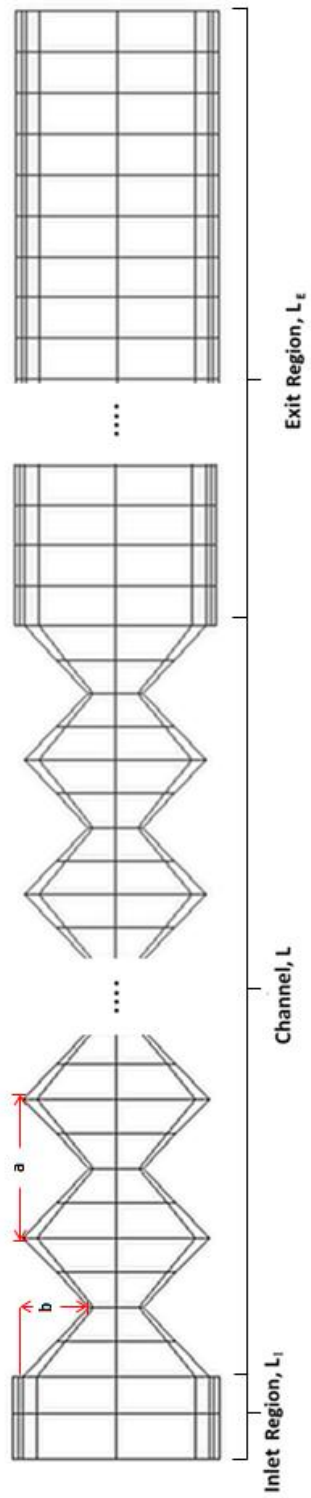


Figure 3-1. Two-dimensional, single channel mesh.

Originally, a single channel model was developed with an entrance height of H_A that utilized symmetry boundary conditions on the upper and lower edges of the inlet and exit regions. However, the results were not physically realizable. Periodic boundary conditions were found to be necessary to achieve the physically realizable results seen in the array model. As a result, the entrance height had to be increased to maintain symmetry.

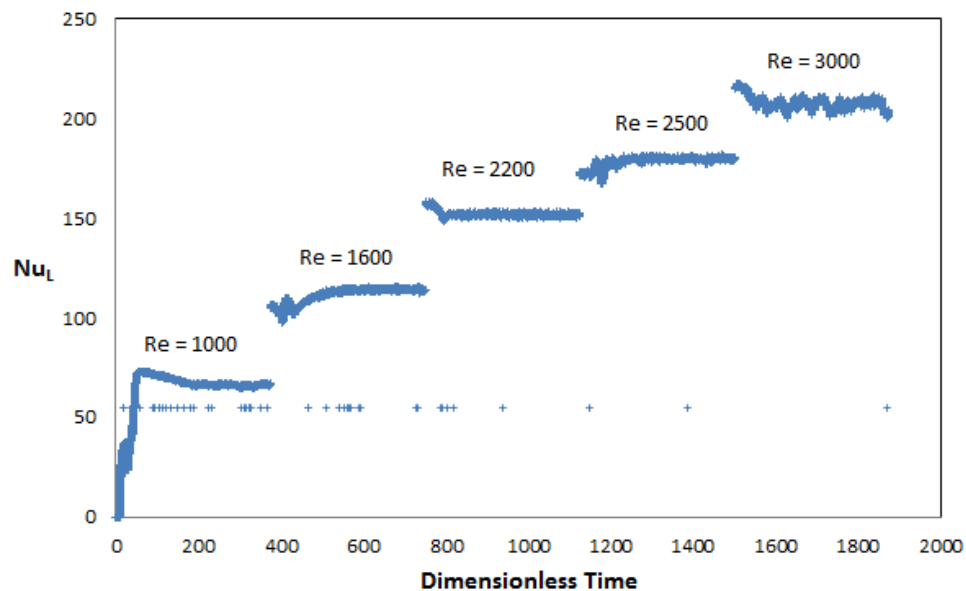


Figure 3-2. Total average Nusselt number versus dimensionless time.

The two-dimensional, single channel model was investigated at $Re = 1000, 1600, 2200, 2500$ and 3000 . Once the simulations had reached steady-state conditions, the average Nusselt number and dimensionless fan power were calculated and compared to the two-dimensional array results. Figure 3-2 shows the total average Nusselt number versus dimensionless time, where dimensionless time is the time for a fluid particle to move one dimensionless unit at a dimensionless axial velocity of one. Once the lowest Reynolds number (1000) reached steady-state conditions, the final result

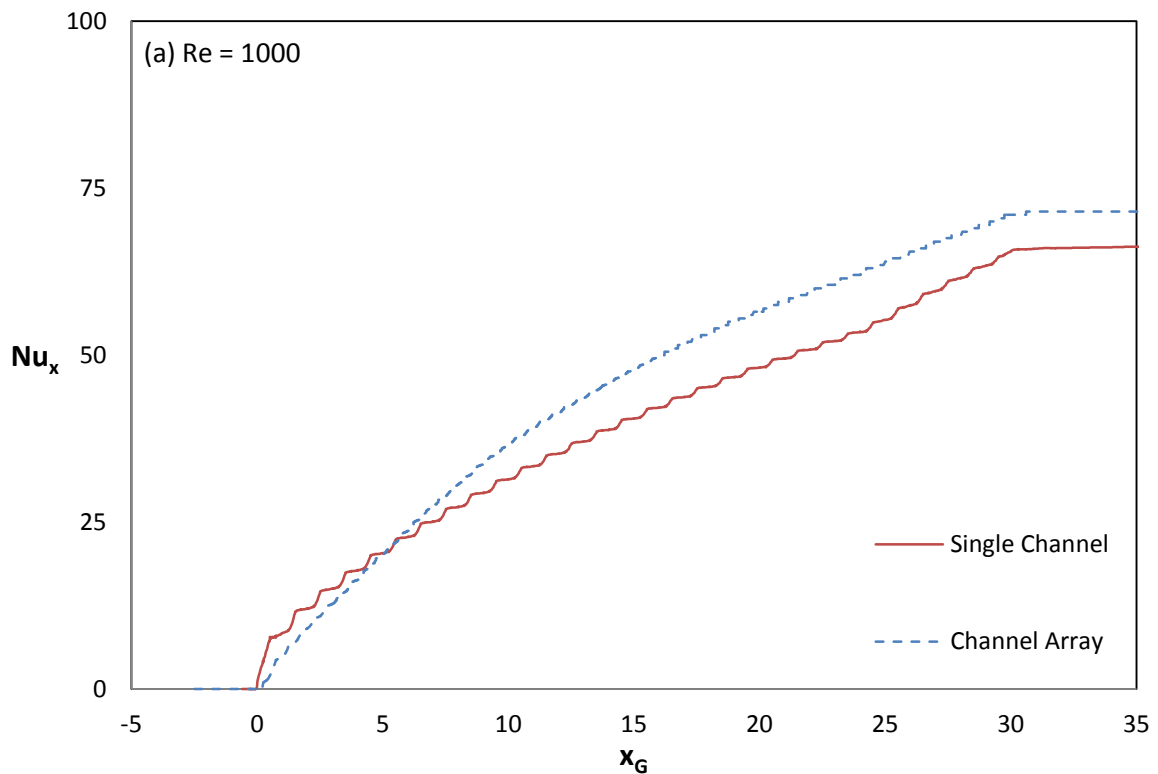
was used as an initial condition for the subsequent Reynolds number. This method is used to achieve results in shorter wall-clock time.

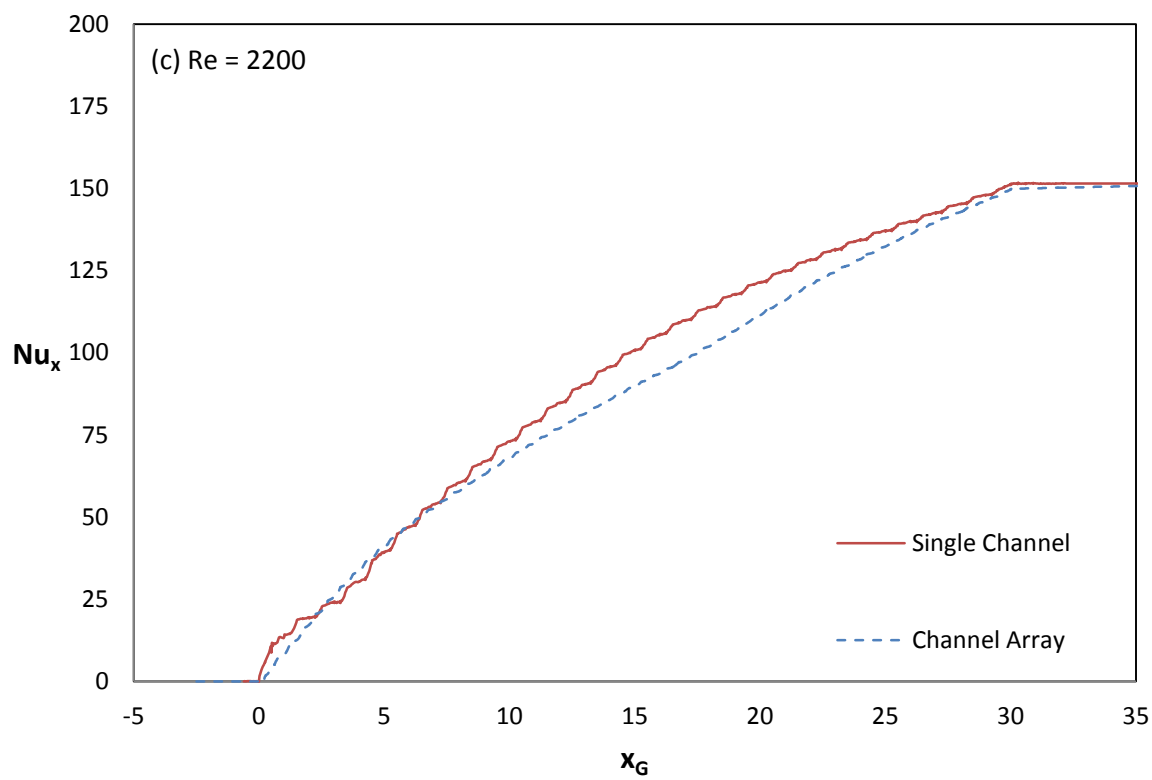
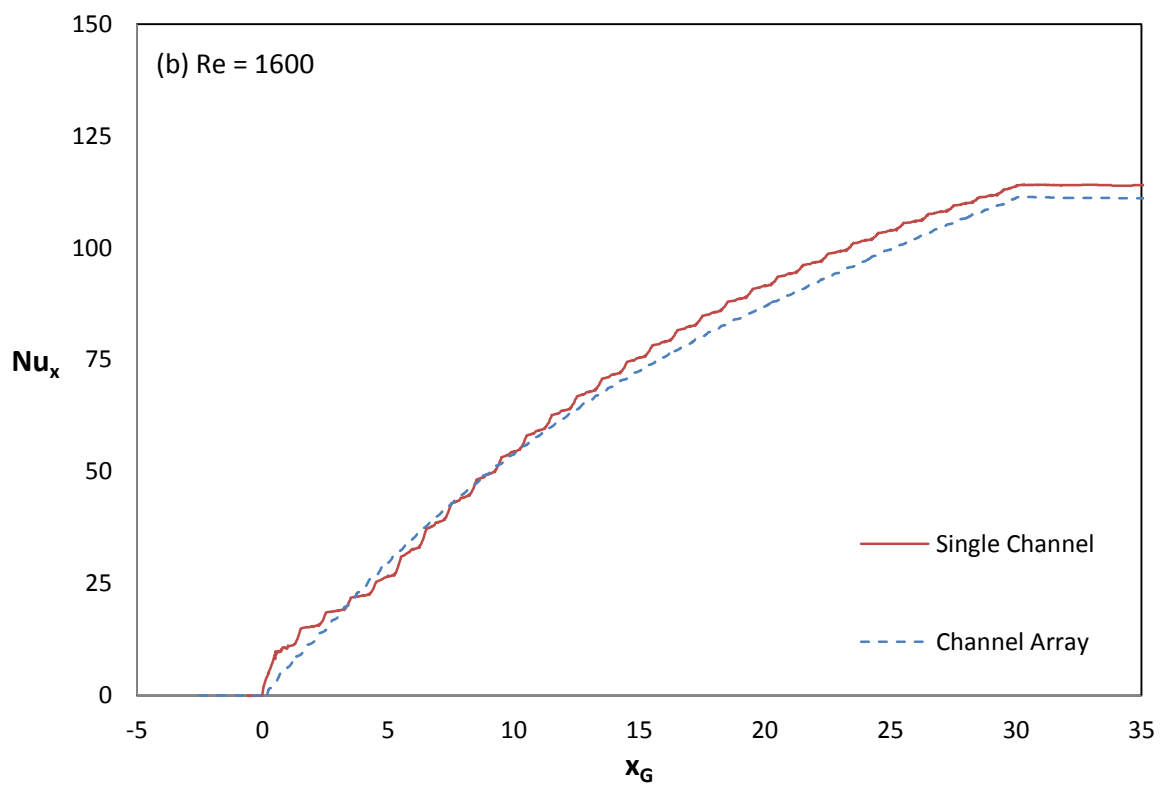
3.2 Heat Transfer Comparison

The average Nusselt number as defined in equation (3) is calculated in a similar method as with the array model. However, since only two heated walls are present in the single channel model, an adjustment was made to the calculation to reflect this difference and is defined as follows.

$$Nu_x = \frac{\int_B^T (\overline{uT})_x dy}{2\alpha} \quad (9)$$

Figure 3-3 shows the average Nusselt number versus groove coordinate comparing the single channel and array channel models at each Reynolds number investigated.





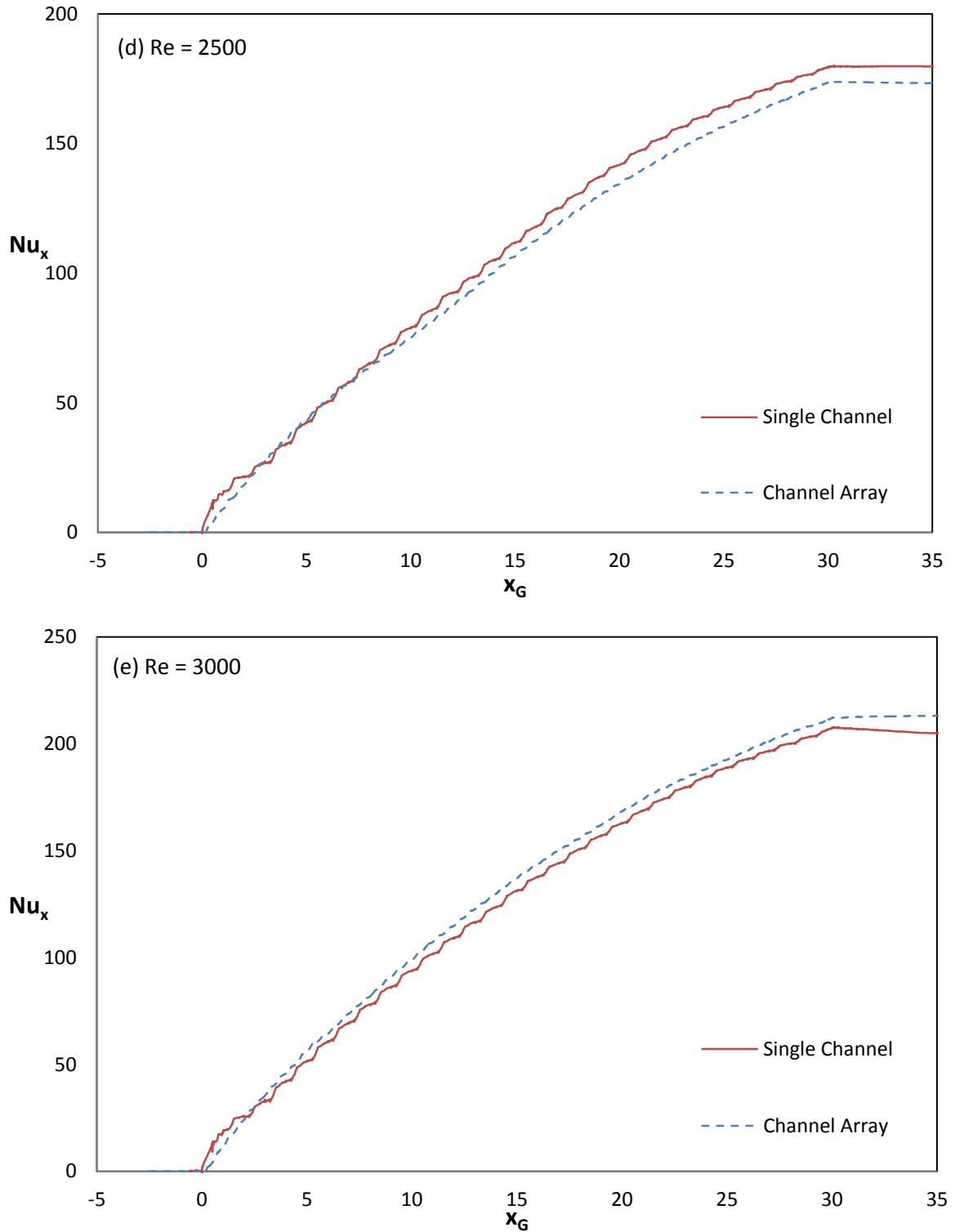


Figure 3-3. Average Nusselt number array and single channel comparison (a) Re = 1000; (b) Re = 1600; (c) Re = 2200; (d) Re = 2500; (e) Re = 3000

Figure 3-3 shows that the average Nusselt number in the single channel is greater at the channel inlet for all Reynolds numbers. This is likely due to the channel inlet, which contains a full converging section rather than a half converging section in the array model. The average Nusselt number exhibits a similar behavior in the single channel as in the array model. However, the change in curvature that was pointed out in Figure 2-5 for the array models is more pronounced in these single channel results. Although the results are not identical, the difference is expected due to the slight difference in passage geometry. The percent difference between the results can be seen in Table 3-1.

Table 3-1. Single channel and channel array average Nusselt number percent difference.

Re	Percent Difference
1000	-8.01%
1600	2.27%
2200	0.93%
2500	3.48%
3000	-2.12%

The percent difference was calculated at $x_G = 30$, or at the total average Nusselt number. The differences are small enough that this model can be used a basis for the three-dimensional simulations.

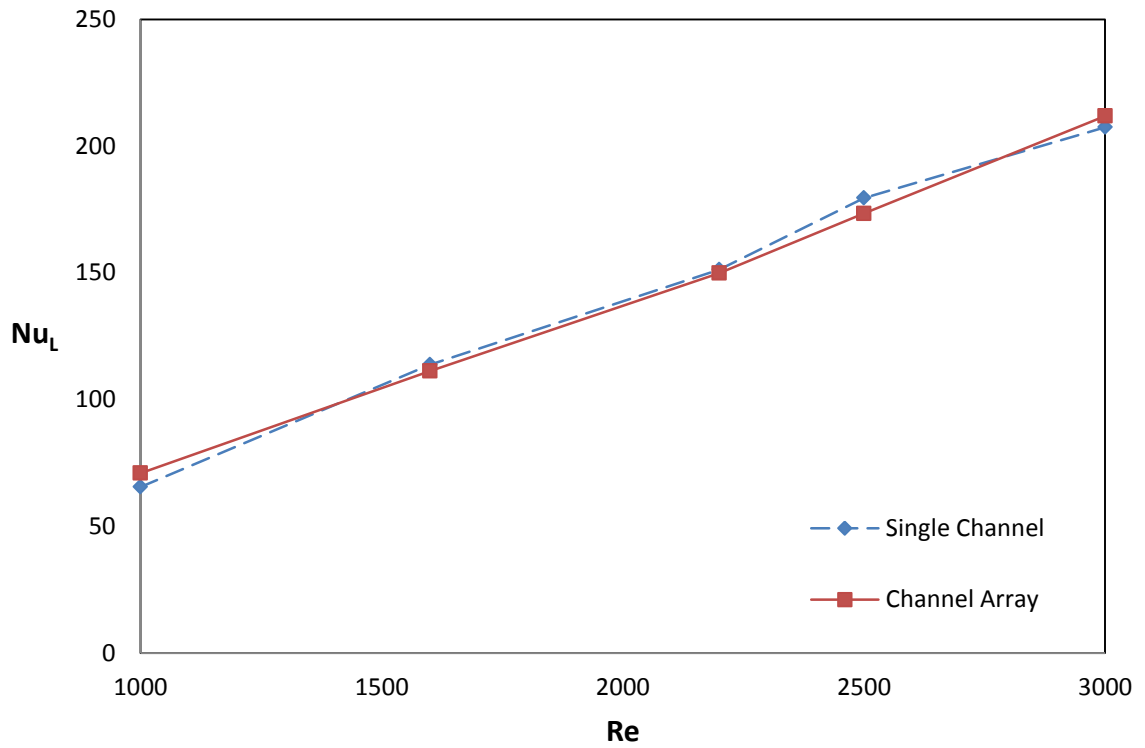
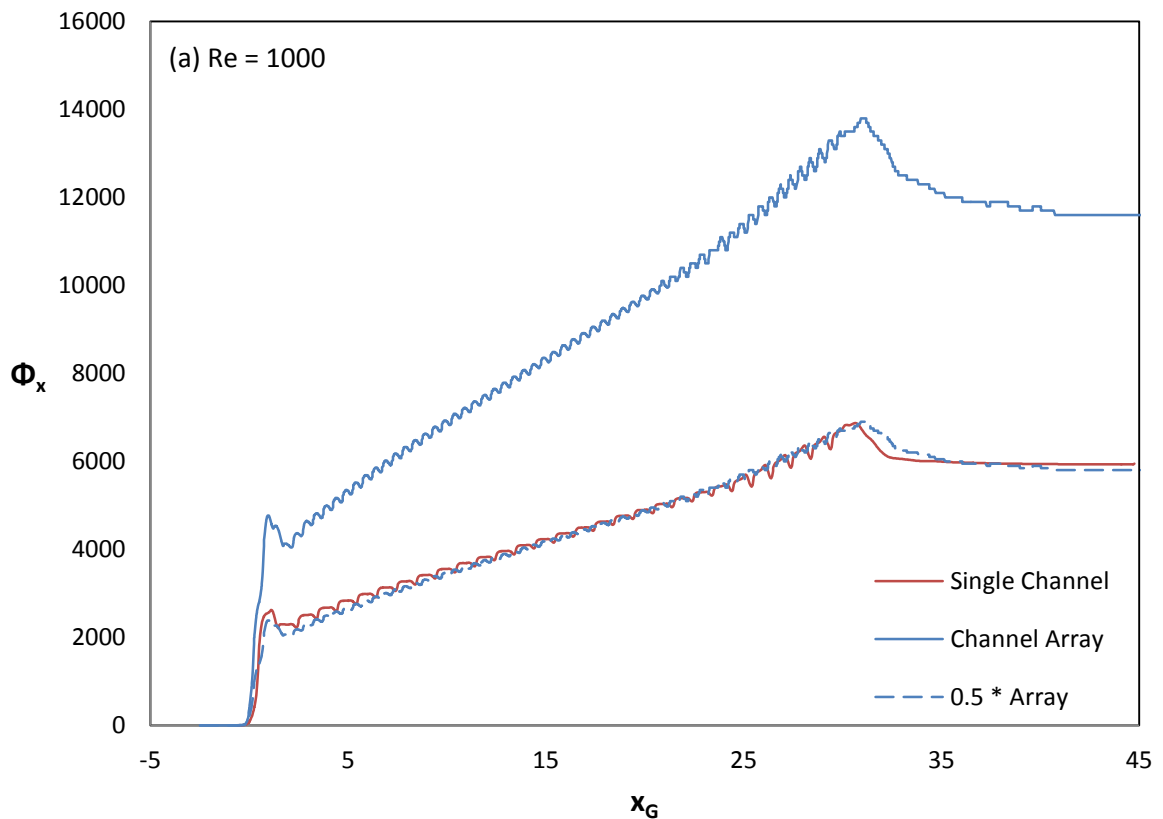


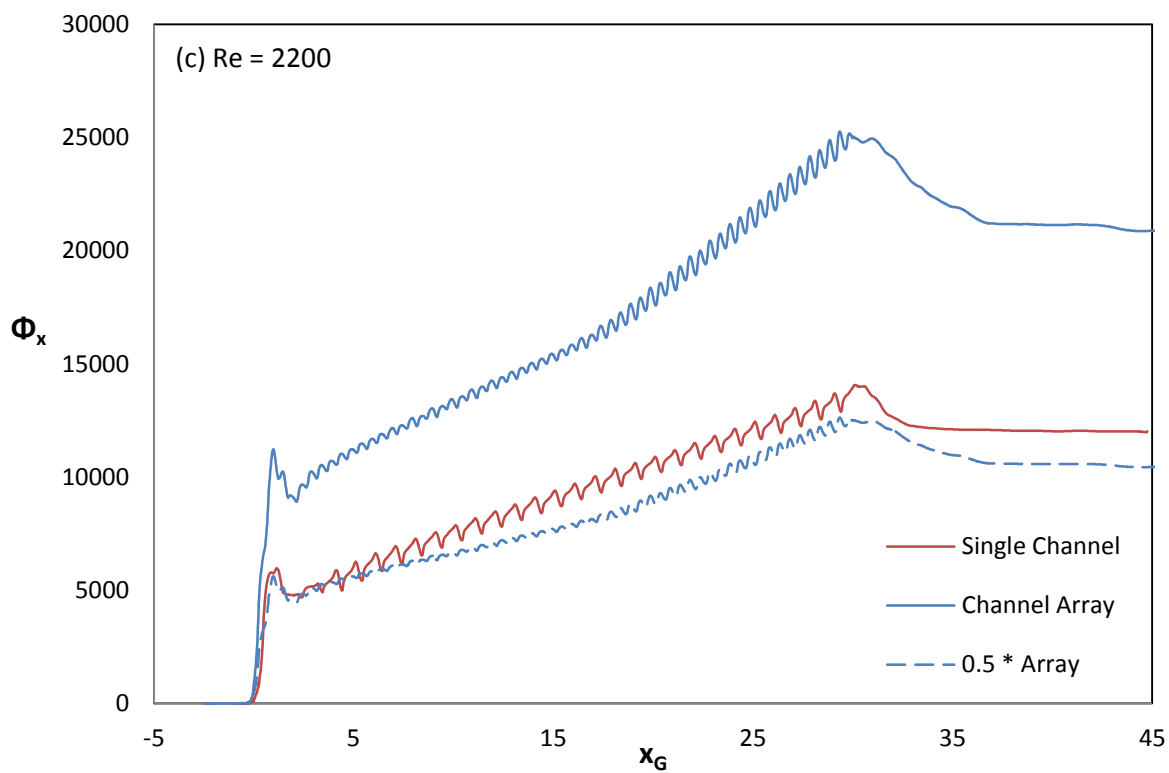
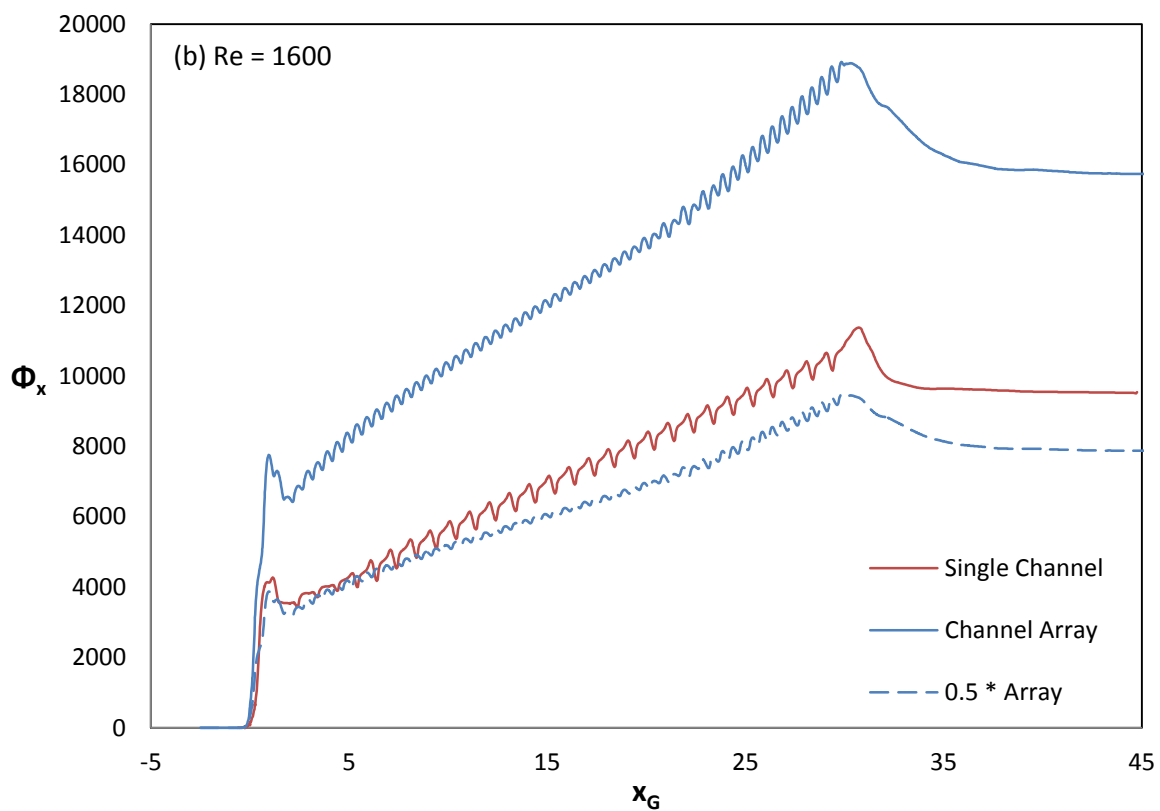
Figure 3-4. Total average Nusselt number array and single channel comparison.

Figure 3-4 shows the total average Nusselt number, Nu_L , versus Reynolds number for both the single channel and the channel array. Again, the results are nearly equal, and the single channel result is not consistently greater than or less than the channel array result.

3.3 Fan Power Comparison

The dimensionless fan power results from the single grooved channel model were also compared with the results from the grooved channel array model. The dimensionless fan power as defined in equation (12) is calculated in the same method as with the array model. Figure 3-5 shows the dimensionless fan power versus groove coordinate comparing the single channel and array channel models at each Reynolds number investigated. Each plot contains the single channel result (red), the channel array result (blue), and one half the channel array result (dashed blue). The channel array result is multiplied by one half to reflect the reduction in the number of passages from two to one.





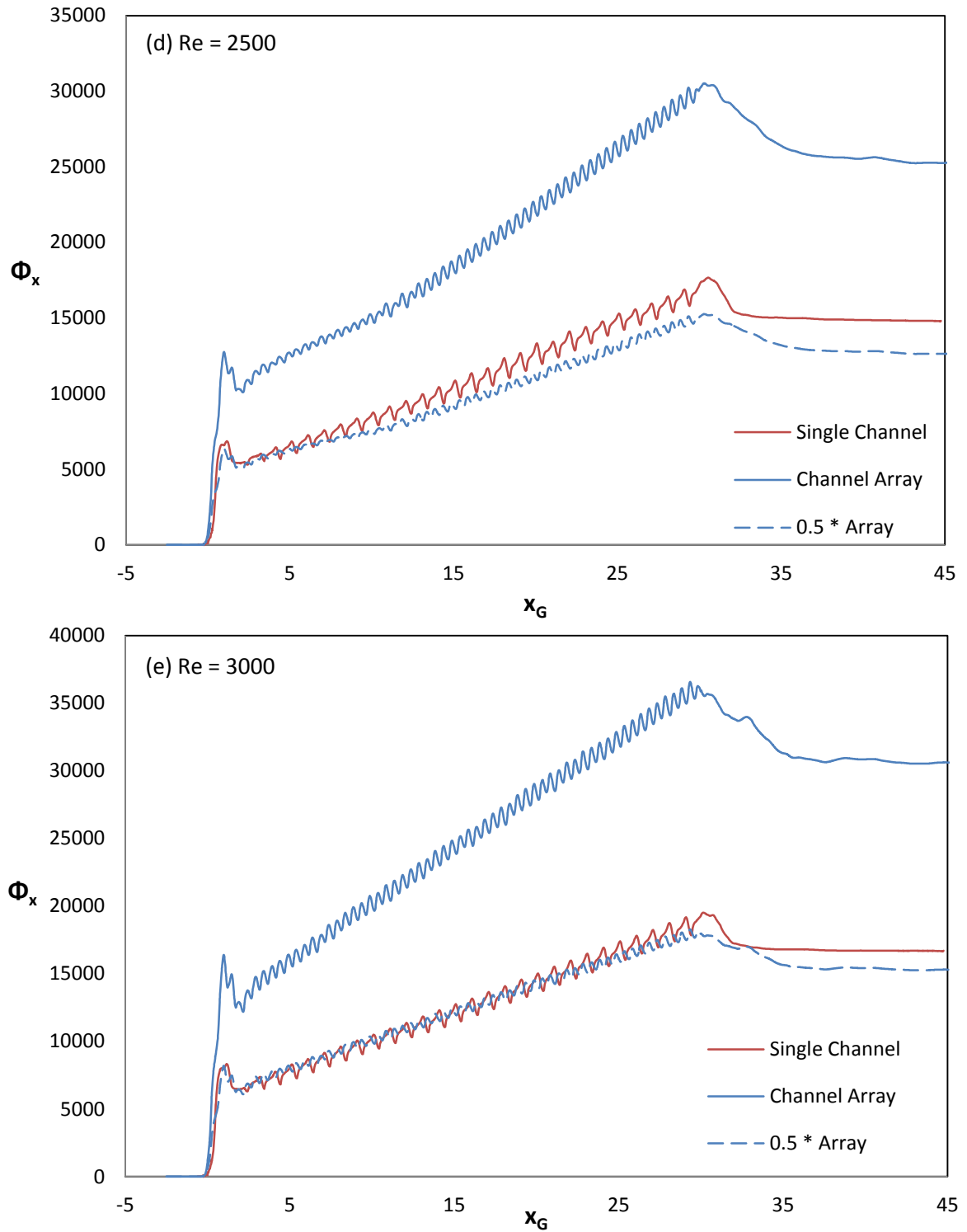


Figure 3-5. Non-dimensional fan power array and single channel comparison (a) Re = 1000; (b) Re = 1600; (c) Re = 2200; (d) Re = 2500; (e) Re = 3000

As expected, the non-dimensional fan power result from the grooved channel array is roughly twice that of the single channel model at each Reynolds number investigated. The amplitude and number of oscillations are greater in the single channel result than in the array result since the grooves are out of phase between the upper and lower passages in the array model. The single channel result is consistently greater than half the channel array results for each Reynolds number. Table 3-2 shows the percent difference between the single channel full channel non-dimensional fan power (evaluated at $x_G = 45$) and channel array full channel non-dimensional fan power.

Table 3-2. Single channel and channel array non-dimensional fan power percent difference.

Re	Percent Difference
1000	2.17%
1600	18.82%
2200	13.74%
2500	15.69%
3000	8.45%

The percent difference for the total non-dimensional fan power is generally greater than for the total average Nusselt number. This indicates that the added effect of multiple channels is not negligible when analyzing the required fan power. Also, the change in outlet geometry may also affect the pressure recovery in the exit region.

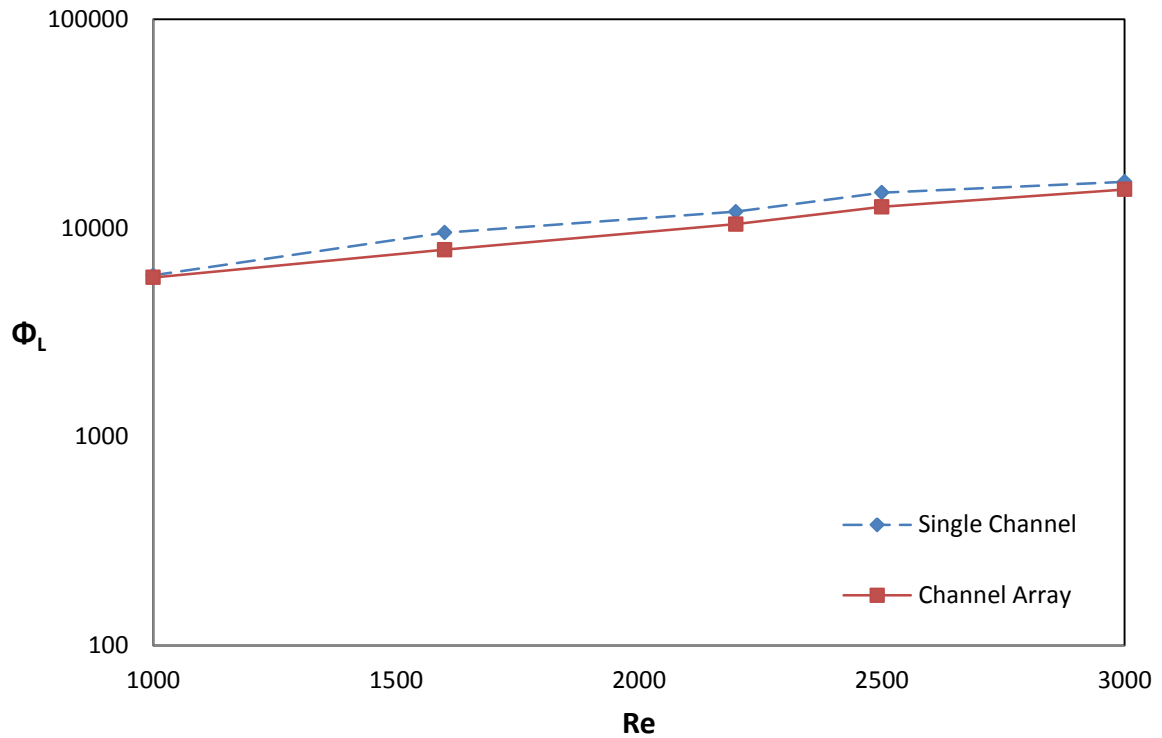


Figure 3-6. Total fan power array and single channel comparison.

Figure 3-6 shows the total fan power, Φ_L , versus Reynolds number for both the single channel and the channel array. These results are close for some Reynolds numbers investigated but further apart for others. The single channel result is consistently greater than the channel array result, but not by a regular margin. Further studies should be performed to analyze the pressure drop in the exit region following a grooved passage or passages.

Chapter 4: Conclusions and Recommendations

4.1 Conclusions

Two-dimensional simulations of forced convection in an array of finite-length, continuously grooved passages with developing flow were performed using the spectral element method for Reynolds numbers ranging from 1000 to 3000. The average Nusselt number and fan power were calculated in order to analyze performance of a grooved passage array compared with a flat passage array.

The temperature and velocity fields develop a shorter distance from the inlet in the grooved passage arrays than in flat-wall arrays. The addition of transverse grooves to the parallel passage arrays introduces unsteadiness a number of grooves downstream of the channel entrance. This onset location moves closer to the channel entrance as the Reynolds number increases. The unsteadiness improves the overall heat transfer compared with a flat passage array of equal average channel height by a factor of 1.46 at $Re = 1000$ and a factor of 2.75 at $Re = 3000$. However, the grooves also cause an increase in the required fan power by a factor of 8.56 at $Re = 1000$ and a factor of 18.10 at $Re = 3000$. As a result, these two-dimensional results show that heat transfer cannot be enhanced without increases the required fan power in the developing regions in the short array.

A two-dimensional comparison between a single grooved channel and a grooved channel array shows that the heat transfer results are comparable per channel. However,

the pressure recovery in the exit region can differ up to 18% suggesting that the effects of neighboring passages play a role in the pressure recovery.

4.2 Recommendations

This study did provide some preliminary results in the effects of transverse surface grooves on developing flow in ducts. However, these two-dimensional results may not adequately capture the entire instability and mixing structures that have been seen in experiments and three-dimensional simulations. Although a three-dimensional spectral element model was constructed, the investigation of this model is beyond the scope of this current work. This model could be used in further work to study the effects of transverse surface grooves on developing flow in ducts. The development of this model is described in section 4.3. Additional analysis tools could also be used to fully describe the two-dimensional array model. These tools could include a root-mean-square velocity analysis to quantitatively describe the onset location of oscillatory flow. Also, the volumetric flow rate, average Nusselt number, and fan power could be found for the individual passage in the array to determine the differences between upper and lower passages. Heat transfer correlations could also be used to verify the numerical flat passage average Nusselt number results in a similar method as was performed for the pressure drop in section 2.6.

Furthermore, the scope of this research did not fully investigate the effects of neighboring passages on the pressure recovery in the exit region. Due to the boundary condition limitations, identical grooved passages could not be compared. However, since some differences were noted in the comparisons that were made, further work in this area

could be particularly interesting. Additionally, pressure drop analyses (as in section 2.6) should be performed for all Reynolds numbers considered.

It is possible that the transverse grooves studied by Greiner et al. and again in this work are not ideal for developing flow. A study should be performed to analyze the effects of groove depth b on the required fan power and heat transfer enhancement with developing flow.

4.3 Recommended Three-Dimensional Model

A three-dimensional spectral element mesh was developed to study the three-dimensional instabilities that were seen in previous experiments. This was accomplished using the two-dimensional, single channel mesh shown in Figure 3-1. Using a Nek5000 program, the mesh was extruded in the z -direction using six equal elements in that span-wise direction. Periodic boundary conditions were also applied in the z -direction. Figure 4-1 shows an isometric view of the three-dimensional, single channel model.

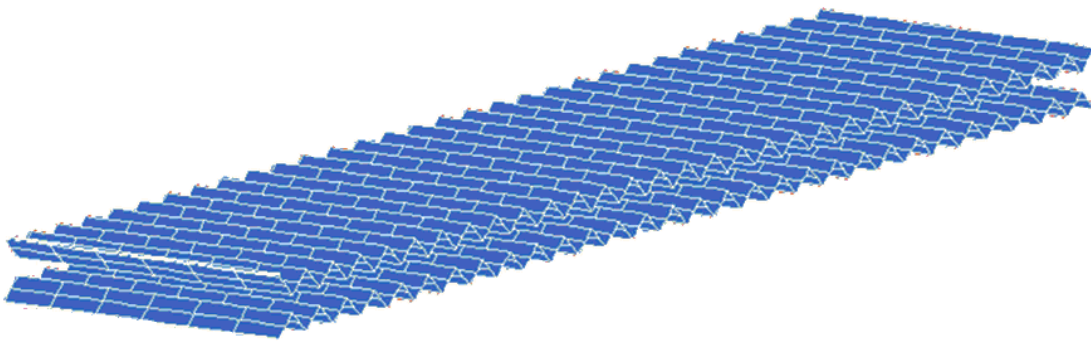


Figure 4-1. Isometric view of three-dimensional, single channel mesh boundary.

This figure only shows the upper and lower boundaries of the three-dimensional computational domain so that the domain is easier to see. Figure 4-1 shows the six equally-spaced elements in the span-wise direction. Furthermore, the exit region that can be seen in Figure 3-1 was removed from the three-dimensional domain due to the inconsistencies in fan power results for the single channel and to speed up the computational time. Fluid with a Prandtl number of 0.7 enters an inlet region from the left side of the domain with a uniform, non-dimensional temperature and velocity. The length of the inlet region is $0.6a$. Like the single channel model in Figure 3-1, the three-dimensional model has thirty grooves with the upper and lower walls modeled using no-slip boundary conditions and a constant wall temperature. The fluid exits the channel (and the domain) using the same special outflow boundary condition that was used in both the channel array model and the two-dimensional single channel model.

Once this model has been analyzed using the heat transfer and fan power performance metrics used on the two-dimensional models, it is suggested that a three-dimensional model of the grooved passage array is constructed to complete the array analysis.

References

- [1] Webb, R.L., 2005, Principles of Enhanced Heat Transfer, second edition, Taylor & Francis, New York.
- [2] Ghaddar, N.K., Korczak, K., Mikic, B.B., and Patera, A.T., 1986a, "Numerical Investigation of Incompressible Flow in Grooved Channels. Part 1: Stability and Self-Sustained Oscillations," *J. Fluid Mech.*, Vol. 163, pp. 99-127.
- [3] Ghaddar, N.K., Korczak, K., Mikic, B.B., and Patera, A.T., 1986b, "Numerical Investigation of Incompressible Flow in Grooved Channels. Part 2: Resonance and Oscillatory Heat-Transfer Enhancement," *J. Fluid Mech.*, Vol. 168, pp. 541-567.
- [4] Greiner, M., Chen, R.F., and Wirtz, R.A., 1991, "Enhanced Heat Transfer/Pressure Drop Measured from a Flat Surface in a Grooved Channel," *J. Heat Transfer*, Vol. 113, pp. 498-501.
- [5] Roberts, E.P.L., 1994, "A Numerical and Experimental Study of Transition Processes in an Obstructed Channel Flow," *J. Fluid Mech.*, Vol. 260, pp. 185-209.
- [6] Karniadakis, G.E., Mikic, B.B., and Patera, A.T., 1988, "Minimum-Dissipation Transport Enhancement by Flow Destabilization: Reynolds Analogy Revisited," *J. Fluid Mech.*, Vol. 192, pp. 365-391.

- [7] Kozlu, H., Mikic, B.B., and Patera, A.T., 1988, "Minimum-Dissipation Heat Removal by Scale-Matched Flow Destabilization," *Int. J. Heat Mass Transfer*, Vol. 31, pp. 2023-2032.
- [8] Amon, C.H., Majumdar, D., Herman, C.V., Mayinger, F., Mikic, B.B. and Sekulic, D.P., 1992, "Experimental and Numerical Investigation of Oscillatory Flow and Thermal Phenomena in Communicating Channels," *Int. J. Heat Mass Transfer*, Vol. 35, pp. 3115-3129.
- [9] Greiner, M., Ghaddar, N.K., Mikic, B.B., and Patera, A.T., 1986, "Resonant Convective Heat Transfer in Grooved Channels," *Proc. Eighth Int. Heat Trans. Conf.*, Vol. 6, p. 2867-2872.
- [10] Sobey, I.J., 1980, "On Flow through Furrowed Channels. Part 1: Calculated Flow Patterns," *J. Fluid Mech.*, Vol. 96, pp. 1-26.
- [11] Stephanoff, K.D., Sobey, I.J., and Bellhouse, B.J., 1980, "On Flow through Furrowed Channels. Part 2: Observed Flow Patterns," *J. Fluid Mech.*, Vol. 96, pp. 27-32.
- [12] Greiner, M., 1987, "Flow Field Destabilization and Heat Transfer in Grooved Channels," ASME FED-Vol. 52, pp. 131-138.
- [13] Greiner, M., Chen, R.F. and Wirtz, R.A., 1990, "Heat Transfer Augmentation through Wall Shape Induced Flow Destabilization," *J. Heat Transfer*, Vol. 112, No. 2, pp. 336-341.

- [14] Chen, R.F., 1993, "Experimental Investigation of Passive Flow Destabilization and Heat Transfer Enhancement in Grooved Channels," Doctor of Philosophy dissertation, University of Nevada, Reno, NV, June 1993.
- [15] Greiner, M., Spencer, G., and Fischer, P.F., 1998, "Direct Numerical Simulation of Three-Dimensional Flow and Augmented Heat Transfer in a Grooved Channel," *J. Heat Transfer*, Vol. 120, pp. 717-723.
- [16] Greiner, M., Faulkner R.J., Fischer, P.F., and Wirtz, R.A., 1997, "Simulations of Three-Dimensional Flow and Augmented Heat Transfer in a Symmetrically Grooved Channel with Constant Temperature Walls," *J. Heat Transfer*, Vol. 122, pp. 653-660.
- [17] Greiner, M., Fischer, P.F., Tufo, H.M., and Wirtz, R.A., 2002, "Three Dimensional Simulations of Enhanced Heat Transfer in a Flat Passage Downstream from a Grooved Channel," *J. Heat Transfer*, Vol. 124, pp. 169-176.
- [18] Greiner, M., Fischer, P.F. and Tufo, H.M., 2002, "Two-Dimensional Simulations of Enhanced Heat Transfer in an Intermittently Grooved Channel," *J. Heat Transfer*, Vol. 124, pp. 538-545.
- [19] Wirtz, R.A., Huang, F., and Greiner, M., 1999, "Correlation of Fully Developed Heat Transfer and Pressure Drop in a Symmetrically Grooved Channel," *J. Heat Transfer*, Vol. 121, pp. 236-239.
- [20] Drazin, P.G., and Reid, W.H., 1981, *Hydrodynamic Stability*, Cambridge University Press, Cambridge, United Kingdom.

- [21] White, F.M., 1991, *Viscous Fluid Flow*, second edition, McGraw-Hill, New York, pp. 291-293.
- [22] SPX Cooling Technologies, 2012, "Indirect Natural Draft Dry Cooling," Retrieved Dec. 6, 2011, from http://www.spx.com/en/images/A4_DRY-IDCT-12_tcm20-35900.pdf.
- [23] Ridouane, E.H. and Campo, A., 2007, "Heat Transfer and Pressure Drop Characteristics of Laminar Air Flows Moving in a Parallel-Plat Channel with Transverse Hemi-Cylindrical Cavaties," *Int. J. Heat Mass Transfer*, Vol. 50, pp. 3913-3924.
- [24] Ridouane, E.H. and Campo, A., 2008, "Heat Transfer Enhancement of Air Flowing Across Grooved Channels: Joint Effects of Channel Height and Groove Depth," *J. Heat Transfer*, Vol. 130, 021901.
- [25] Herman, C. and Kang, E., 2002, "Heat Transfer Enhancement in a Grooved Channel with Curved Vanes," *Int. J. Heat Mass Transfer*, Vol. 45, pp. 3741-3757.
- [26] McGarry, M., Campo, A. and Hitt, D.L., 2004, "Numerical Simulations of Heat and Fluid Flow in Grooved Channels with Curved Vanes," *Numer. Heat Transfer, Part A*, Vol. 46, pp. 41-54.
- [27] Patera, A.T., 1984, "A Spectral Element Method for Fluid Dynamics; Laminar Flow in a Channel Expansion," *J. Comput. Phys.*, Vol. 54, pp. 468-488.

- [28] Fischer, P.F., 1997, "An Overlapping Schwarz Method for Spectral Element Solution of the Incompressible Navier-Stokes Equations," *J. of Comput. Phys.*, Vol. 133, pp. 84-101.
- [29] Fischer, P.F. and Patera, A.T., 1991, "Parallel Spectral Element Solutions of the Stokes Problem," *J. Comput. Phys.*, Vol. 92, pp. 380-421.
- [30] Fischer, P.F. and Patera, A.T., 1992, "Parallel Spectral Element Solutions of Eddy-Promoter Channel Flow," *Proc. of the European Research Community on Flow Turbulence and Computation Workshop*, Lausanne, Switzerland, Cambridge University Press, pp. 246-256.
- [31] Fischer, P.F. and Ronquist, E.M., 1994, "Spectral Element Methods for Large Scale Parallel Navier-Stokes Calculations," *Comp. Meth. Mech. Engr.*, pp. 69-76.
- [32] Fischer, P.F., Lottes, J.W., and Kerkemeier, S.G., 2008, "Nek5000 Web Page," <http://nek5000.mcs.anl.gov>.
- [33] Fox, R.W., and McDonald, A.T., 1985, *Introduction to Fluid Mechanics*, third edition, John Wiley & Sons, New York, p. 338.
- [34] Kays, W.M., and London, A.L., 1964, *Compact Heat Exchangers*, second edition, McGraw-Hill, New York, pp. 32-33.
- [35] White, F.M., 1991, *Viscous Fluid Flow*, second edition, McGraw-Hill, New York, pp. 291-293.